applied sciences

MDPI

Article

Comparative Analysis of the Cooling Efficiency in Tropical Climate of Three Alternative Materials for Evaporative Cooling Pads

Felipe Andrés Obando Vega [1,*], Ana Paola Montoya Rios [1], Jairo Alexander Osorio Saraz [1], Flávio Alves Damasceno [2] and Matteo Barbari [3]

[1] Facultad de Ciencias Agrarias, Universidad Nacional de Colombia, Medellín 050034, Colombia; apmontoy@unal.edu.co (A.P.M.R.); aosorio@unal.edu.co (J.A.O.S.)
[2] Department of Engineering, Federal University of Lavras, Lavras 37200-000, Brazil; flavio.damasceno@ufla.br
[3] Department of Agriculture, Food, Environment and Forestry, University of Firenze, 50145 Firenze, Italy; matteo.barbari@unifi.it
* Correspondence: faobando@unal.edu.co

Featured Application: The findings are highly relevant for the design and manufacture of evaporative cooling pad with alternative materials.

Abstract: A comparison between commercial cellulose evaporative cooling pad and pads manufactured with three alternative materials was made for environmental conditions typical of tropical countries. Wind tunnel tests were carried out to compute the convective heat and mass transfer coefficients and to measure the pressure drop across each pad, obtaining expressions that can be used as reference for future simulations. Using a mathematical model, a detailed analysis of the efficiency, Temperature–Humidity Index, temperature drop and relative humidity through the pads was performed in terms of different operative and constructive conditions, such as air velocities, dry-bulb temperatures, relative humidity and pad thickness. Significant differences between the pressure drop across the pads were found, which increases with the inlet air velocity and water flow. A weak relation between the analysed variables and the inlet air velocity was found, while a high correlation between the analysed variables, pad thickness and the external environmental conditions was established. Cooling efficiencies above 40% and a Temperature–Humidity Index below the mild zone of thermal stress were obtained for the alternative panels. Although the cellulose cooling pad showed the best behaviour in all aspects, the alternative pads can be used as substituted in specific applications to reduce the Temperature–Humidity Index inside agricultural facilities.

Keywords: cooling pad; cellulose; evaporative cooling; alternative materials; cooling efficiency; temperature–humidity index

Citation: Obando Vega, F.A.; Montoya Rios, A.P.; Osorio Saraz, J.A.; Damasceno, F.A.; Barbari, M. Comparative Analysis of the Cooling Efficiency in Tropical Climate of Three Alternative Materials for Evaporative Cooling Pads. *Appl. Sci.* **2022**, *12*, 77. https://doi.org/10.3390/app12010077

Academic Editor: Andrea Frazzica

Received: 7 November 2021
Accepted: 17 December 2021
Published: 22 December 2021

1. Introduction

Evaporative cooling is one of the most efficient methods for cooling agro-industrial facilities [1,2]. The air from outside the facility is forced to enter through a constantly wet porous medium (pad). Sensible and latent heat transfer occurs when the air is in contact with the water surface. Air loses sensible heat, decreasing its temperature, while water evaporates from the surface of the pad, increasing the humidity of the air and adding latent heat. The air at the outlet of the pad has a lower temperature and a higher relative humidity than the inlet one. However, the high cost of the traditional cellulose pad makes the implementation of this technique unfeasible in small and medium agro-industrial production systems. This has prompted research on alternative materials that could be used to manufacture pads at a fraction of the cost of cellulose ones [3,4]. Alternative materials have been selected based on the local availability, low acquisition costs and final disposal, the ones that comes as waste from other productive process, lowing their

environmental impact being preferred. Tables 1 and 2 summarize the cooling efficiency (η) of some alternative materials that have been previously analysed, which include natural, mineral and synthetic sources; the use of natural fibres has predominated.

Table 1. Cooling efficiency (η) of cooling pad research studies based on organic raw materials.

Raw Material	Research	η [%]
Aspen fibres media	[5–8]	71.6–97.7
Coconut coir fibre	[6,7,9–14]	50.8–92.86
Expanded clay	[15,16]	42.0–83.0
date palm fibre	[17]	38.9
Eucalyptus fibre	[18,19]	23.0–76.0
Jute fibre	[17,20–22]	57.0–87.0
Khus fibre	[7,11,12,14]	64.2–82.0
Luffa fibre	[12,17]	55.1–73.7
Palash fibres	[7]	81.0
Rice straw	[23]	31.0–79.0
Sackcloth	[24]	69.0
Slice woods	[25]	76.0
Straw fibre	[24,25]	71.9–90.0
Wood savings	[9]	25.0–65.8
Wood wool	[9,11,12]	74.2–92.2

Table 2. Cooling efficiency (η) of cooling pad research studies based on inorganic raw materials.

Raw Material	Research	η [%]
Cyprus marble	[19]	15.0–34.0
Dry bulrush basket	[19]	19.0–35.0
Fabric PVC sponge	[26]	76.7–91.6
Galvanized metal sheets	[12]	83.0
Greenhouse shading net	[27]	25.2–32.8
High density polyethylene plastic	[8,28]	70.0–94.0
Metal sheets	[24]	71.8
Non-woven fabric perforated	[13]	48.3–89.3
Polypropylene hollow fibres	[29]	73.0
Pottery tubular rods	[30]	49.4–56.9
Pumice stones	[27]	56.1–91.6
Stainless steel wire mesh	[11,12]	50.0–85.2
Volcanic tuff	[27]	68.0–77.9
Ceramic pipes	[12,19]	72.0
Yellow stones	[19]	18.0–49.0

The cooling efficiency is affected by the inlet air velocity and the pad thickness, in addition to the influence of the external thermal conditions [31]. However, conducting experimental tests to assess the influence of all factors on cooling efficiency is a time and resource consuming task. Some phenomenology mathematical models had been proposed and validated through experimental tests [32,33] to address this issue, determining the behaviour of the pad under different environmental, operating and manufacturing conditions. This has been done exhaustively for cellulose pads, nevertheless, the main difficulty that arose for alternative materials is the computation of their convective heat and mass transfer coefficients, in addition to the computation of the air–water contact surface area. In this matter, Liao et al. [13] proposed to scale the Hilper correlations [34] by the quotient between the characteristic length (l_e) and thickness (L) of the pad. This was validated later by [32,35,36] for pads manufactured with cellulose, showing good agreement between the experimental and numerical results. Moreover, few authors have reported the convective heat and mass transfer coefficients or the characteristic length [7,13,21,26,30,33], making it difficult to develop future simulations of the same material under different conditions.

Alternative materials with cooling efficiencies above 70% were found (Tables 1 and 2), which is similar for the cellulose pad. However, most of these experimental tests had been conducted in favourable thermal conditions for evaporative cooling, high dry-bulb temperature and low relative humidity [8]. Hence, this has led to wondering whether the alternative materials are suitable for a particular location or specific thermal conditions [3,25,26,37–43], for example, in low dry-bulb temperatures and high relative humidity.

The air pressure drop across the pad is generally omitted in the evaluation of alternative materials. Increasing the pressure drop is equivalent to incrementing the electrical power required by the exhaust fans of the facility, leading to high operating costs. Research studies have reported values between 9 Pa [27] and 365.5 Pa [21], higher than the reported values for the cellulose pad (<40 Pa) [36,44]. For cooling efficiencies above 60%, some authors have reported pressure drops above 100 Pa [13,15,21,27].

The change in the dry-bulb temperature and relative humidity across the pad allows us to characterize the pad cooling efficiency. The change of the relative humidity across the pad is frequently omitted in reports of research results, being one of the variables that most affects the thermal comfort inside the agro-industrial facilities. Using indexes that relate both variables can provide an idea of the impact that the cooling pad has over the microclimatic conditions within the installation. The Temperature–Humidity Index (THI) is an index used frequently to characterize the animal thermal comfort, which provides four levels of thermal stress according to the characteristics of the animals: mild ($68 \leq \text{THI} < 72$), moderate ($72 \leq \text{THI} < 80$), severe ($80 \leq \text{THI} < 90$) and emergency ($\text{THI} \geq 90$) [45] .

A comparison between a commercial cellulose pad and three alternative materials that have not been previously studied in tropical climates is presented in this paper. The influence of the pad thickness, particle size of the material, and dry-bulb temperature, relative humidity and velocity of the inlet air, on the cooling efficiency, THI, dry-bulb temperature drop and the increase in the relative humidity across the pads was analysed, with the objective of finding alternative materials that provide a fluid–thermal behaviour similar to that of the cellulose pad. For this, experimental validation in a wind tunnel and a phenomenological mathematical model of the pads were employed. A methodology based on image processing was also developed to compute the specific wetted surface area of each alternative material. Finally, expressions to compute the convective heat and mass transfer coefficients and the pressure drop across the pads were obtained for each material.

2. Materials and Methods

Three alternative materials: crushed coconut shells (CS), crushed burnt clay hollow brick (BC) and pumice stone (PS), were selected as raw materials to manufacture evaporative cooling pads, according to their availability and low-cost in the subtropical country of Colombia. Their cooling efficiency was compared with the frequently used cellulose cooling pad (CL, Munters Brasil Industria e Comércio Ltda, Araucária, Brazil). Two particle range sizes of coconut shell: 7.93 to 12.7 mm (CS_1) and 12.7 to 19.0 mm (CS_2); one range size of burnt clay hollow bricks: 12.7 to 19.0 mm; and two range sizes of pumice stone: 34.9 to 45.0 mm (PS_1) and 45.0 to 55.5 mm (PS_2), were evaluated. For each material, a pad of 0.5 m of height by 0.5 m of width was manufactured. All the cooling pads had a thickness of 0.1 m (Figure 1). The thickness was selected from a balance between pressure drop and cooling efficiency from previous research [28]. The pads were tested in an instrumented wind tunnel [32], increasing the air inlet velocity (u) from 0.5 m s^{-1} to 3.5 m s^{-1} for the cellulose pad or with the pressure below 160 Pa or until test failure due to water force out of the pad. In addition, three water flows (Q) around the recommended value of 6.2 L min^{-1} m^{-1} [46] were tested: 2, 6.2 and 10 L min^{-1} m^{-1}, to determine their incidence over the pressure drop across the pad.

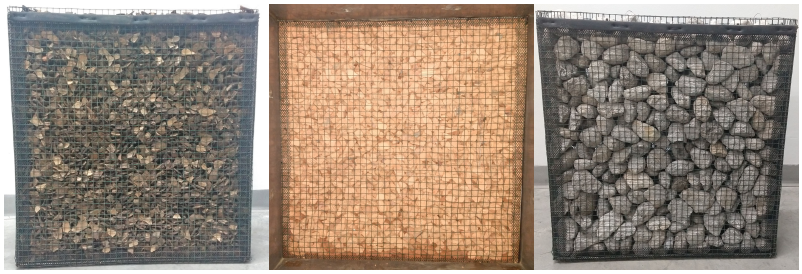

(a) (b) (c)

Figure 1. Photographies of the pad built with the alternative materials. (**a**) Coconut shells pad. (**b**) Burnt clay hollow brick pad. (**c**) Pumice stone pad.

The mathematical model that described the fluid-dynamic and hygrothermal behaviour of cooling pads, proposed by Obando et al. [32], was used in order to compare the behaviour of the pads at different inlet air velocities (u: 0.5 to 2 m^{-1}), thickness of pad (L: 0.05 to 0.15 m) and environmental conditions: dry-bulb temperature (T_{db_i}: 25 to 35 °C) and relative humidity (ϕ_i: 30 to 70%) of the inlet air. Twenty-one equidistant values from the inlet air relative humidity (ϕ_i) interval and 11 values for each one of the other variables were selected, obtaining 307,461 combinations of different conditions to simulate for each pad. The cooling efficiency (η, Equation (1) [46], where T_{db_o} is the air temperature of the outlet air and T_{wb_i} is the wet-bulb temperature of the inlet air), the THI (Equation (2) [45,47]), the change in the dry-bulb temperature (ΔT_{db}) and relative humidity ($\Delta\phi$) across the pads were compared. For this purpose, it was required to quantify the specific surface area (ζ) and the convective heat (h_H) and mass (h_M) transfer coefficients of each pad.

$$\eta = \frac{T_{db_i} - T_{db_o}}{T_{db_i} - T_{wb_i}} \tag{1}$$

$$THI = 0.8T_{db_o} + \frac{\phi_o}{100}(T_{db_o} - 14.3) + 46.3. \tag{2}$$

A specific surface area of 372.6 m^{-1} for the cellulose pad was considered [32]. For the other pads, it was estimated from the geometry of the particles. For the coconut shells and burn clay bricks, it was estimated from processing photographs of the particles, taking advantage of the fact that they present a planar geometry. The pumice stones were approximated to ellipsoids and the surface area was computed using the Knud Thomsen Formulae (A1) and the Dall Equation (A2) [48]. The results obtained with each expression were validated, covering the surface of each stone of a sample of 1000 g with one layer of aluminium foil. To determine the surface area of the aluminium foil, imaging processing was also employed. In Appendix A, the methodology followed is described in detail.

The convective heat and mass transfer coefficients were compute using the correlation of Hilper, modified for cooling pads [13] (Equation (3)).

$$Nu = a_1 \left(\frac{le}{L}\right)^{b_1} Re^{c_1} Pr^{0.37}, \tag{3a}$$

$$Sh = a_2 \left(\frac{le}{L}\right)^{b_2} Re^{c_2} Sc^{0.37}, \tag{3b}$$

where Nu, Re Pr, Sc and Sh were Nusselt, Reynolds, Prantl, Schmidt and Sherwood dimensional numbers, respectively [34]; l_e is the specific length, computed as the inverse of ζ, and L is the thickness of the cooling pad. The a's, b's and c's parameters were fitted using the inlet and outlet air thermal conditions obtained from the experimental test in the wind tunnel for each pad. The convective heat and mass transfer coefficients were then computed using the Nu and Sh definitions as $h_H = Nu \times k \times l_e^{-1}$ and $h_M = Sh \times D_{AB} \times l_e^{-1}$ [34], with

k as the thermal conductivity and D_{AB} as the mass diffusion coefficient. A Wilcoxon rank sum statistical test (*ranksum* function, The MathWorks Inc. (Natick, MA, USA), *MATLAB* 2018a) [49–51] was used to validate the agreement between the experimental data and the predicted thermal conditions of the modelled air outlet. The coefficient of determination (R^2)), the Root Mean Square Error (RMSE) and regression plots of the dry-bulb temperature and relative humidity of the outlet air were also computed.

A porous medium such as the cooling pad is also characterized by its porosity and permeability. Porosity or void fraction (ε) is a measure of the empty spaces between material particles. To determine the porosity of each material, a container of known volume was filled with the material and then water was added to the top of the container. The porosity was then computed using Equation (4). For hygroscopic materials, such as the pumice stone and burnt clay, the recipient was refilled after one hour of test. A porosity of 91.2% was considered for the cellulose pad [36,52].

$$\varepsilon = \frac{\text{Water added}}{\text{Container volume}}. \tag{4}$$

The permeability (K) is an indication of the ability of the air to flow through a porous medium such as the pad. Several expressions had been proposed to relate it to the pressure drop (ΔP) across it and to the air velocity (u) [36,44]. The Darcy–Forchheimer Equation (5) shows a good description of the dynamics of the fluid across the porous medium [53], where β is known as the Forchheimer coefficient.

$$-\frac{\Delta P}{L} = \frac{\mu}{K}u + \rho\beta u^2. \tag{5}$$

To fit Equation (5) to the experimental data, the Least Absolute Residuals (*LAR*) method from the curve fitting toolbox of MATLAB® was used [54].

3. Results

Table 3 summarized the statistical description of the environmental conditions of the inlet air for each pad tested. These presented small changes during the test (below that 0.9 °C and 7.9%), according to the standard deviation values. The alternative pads were tested in similar dry-bulb temperatures of the inlet air (T_{db_i}) with mean values between 25.4 and 27.1 °C and relative humidity (ϕ_i) between 41.0 and 48.7%. T_{db_i} and ϕ_i presented their maximum and minimum values during the cellulose pad tests, respectively.

Table 3. Statistical descriptions of the inlet air dry-bulb temperature (T_{db_i}) and relative humidity (ϕ_i) for the wind tunnel tests. $\bar{T}_{db_i}$ and $\bar{\phi}_i$ are the means, $\tilde{T}_{db_i}$ and $\tilde{\phi}_i$ are the medians, σ is the standard deviation and σ^2 is the variance.

Pad	Temperature				Relative Humidity			
	$\bar{T}_{db_i}$ [°C]	$\tilde{T}_{db_i}$ [°C]	σ [°C]	σ^2 [°C^2]	$\bar{\phi}_i$ [%]	$\tilde{\phi}_i$ [%]	σ [%]	σ^2 [%^{2}]
CL	24.6	24.6	0.5	0.3	62.1	62.5	4.1	16.4
CS_1	26.2	26.4	0.9	0.8	46.5	47.6	7.9	61.6
CS_2	25.4	25.4	0.2	0.1	46.0	46.0	1.3	1.8
BC	25.7	25.7	0.3	0.1	41.7	41.5	1.5	2.3
PS_1	26.9	26.9	0.4	0.2	41.0	41.0	5.3	28.2
PS_2	27.1	27.0	0.5	0.3	48.5	48.7	2.4	5.9

Statistical description of the η and THI of the outlet air are summarized in Table 4. Although the cellulose pad cooling was tested in low T_{db_i} and high ϕ_i, it presented the highest average cooling efficiency, followed by the CS_2 pad. The CS_1, PS_1 and PS_2 pads presented the lowest cooling efficiency considering that they were tested in the highest T_{db_i} and lowest ϕ_i. The lowest average THI value was for the CS_2 and BC pads. The efficiency of the CL pad was slightly above, because it was tested with higher ϕ_i conditions. Through

all experimental tests, ϕ_i had a dispersion up to 7.9%, being significantly lower for CS_2, BC and PS_1 pads. The dispersion of THI was up to 1.6 units for the CS_1 pad and significantly lower for the other pads.

Table 4. Statistical descriptions of the cooling efficiency (η) and the Temperature–Humidity Index (THI) for the wind tunnel tests. $\bar{\eta}$ and $\overline{\mathrm{THI}}$ are the means, $\tilde{\eta}$ and $\tilde{\mathrm{THI}}$ are the medians, σ is the standard deviation and σ^2 is the variance.

Pad	η				THI			
	$\bar{\eta}$ [%]	$\tilde{\eta}$ [%]	σ [%]	σ^2 [%^{2}]	$\overline{\mathrm{THI}}$	$\tilde{\mathrm{THI}}$	σ	σ^2
CL	68.6	68.8	6.0	35.6	68.8	68.8	0.4	0.2
CS_1	45.9	45.9	6.7	45.1	70.6	70.4	1.6	2.6
CS_2	65.1	65.0	1.8	3.3	67.6	67.60	0.2	0.1
BC	56.4	56.6	1.7	2.9	67.9	68.0	0.2	0.1
PS_1	45.2	45.4	1.9	3.6	70.4	70.1	0.8	0.6
PS_2	42.4	41.0	4.0	15.8	72.3	72.4	0.5	0.2

Table 5 summarizes the statistical description of the change in the dry-bulb temperature ($\Delta T = T_{db_i} - T_{db_o}$) and relative humidity ($\Delta\phi = \phi_i - \phi_o$) of the air across the pads. The mean and median of ΔT follow the same behaviour of the ϕ_i, with the highest value for the CS_2 and BC pads. These also present the highest $\Delta\phi$. The lowest $\Delta\phi$ was obtained for the CL pad. In general, the average dry-bulb temperature drop was up to 5.0 °C with a standard deviation of ±1 °C and the increment in ϕ_i was between 21.2% and 35.5% with a standard deviation of ±3.7%.

Table 5. Statistical descriptions of the change in the dry-bulb temperature (ΔT) and relative humidity ($\Delta\phi$) across the pads in the wind tunnel tests. $\overline{\Delta T}$ and $\overline{\Delta\phi}$ are the means, $\widetilde{\Delta T}$ and $\widetilde{\Delta\phi}$ are the medians, σ is the standard deviation and σ^2 is the variance.

Pad	ΔT				$\Delta\phi$			
	$\overline{\Delta T}$ [°C]	$\widetilde{\Delta T}$ [°C]	σ [°C]	σ^2 [°C^2]	$\overline{\Delta\phi}$ [%]	$\widetilde{\Delta\phi}$ [%]	σ [%]	σ^2 [%^{2}]
CL	−3.6	−3.6	0.7	0.4	21.2	21.1	3.7	13.7
CS_1	−3.6	−3.3	1.0	1.1	27.9	27.0	3.6	13.3
CS_2	−5.0	−5.0	0.2	0.1	35.2	35.3	1.4	1.9
BC	−4.8	−4.7	0.2	0.1	32.2	32.0	1.1	1.2
PS_1	−4.0	−4.0	0.5	0.2	25.5	25.5	2.3	5.1
PS_2	−3.2	−3.1	0.4	0.1	22.9	22.8	1.3	1.6

Statistical descriptions of the water temperature entering and leaving the cooling pads are shown in Table 6. The water that entered the pad had an average temperature below 21.1 °C, with a high variability (1.7 °C). The differences between the temperature of the water when entering and leaving the pad were caused by the pump heating. This was more noticeable when low water flows were used in the tests. This also explains the high variability of the water temperature entering the pad. Temperatures of the water leaving the pad were closer and even lower than the inlet air wet-bulb temperature, as was expected from the adiabatic cooling process existing through the wetted pads.

The statistics analysis of the inlet air velocities, which were used in the wind tunnel to test the pads, are summarized in Table 7. The cellulose pad allowed us to evaluate its behaviour for a wider range of velocities (0.5 to 3.5 m s^{-1}). However, the alternative materials, except the CS_1 and BC pads, were tested for three inlet air velocities; 0.5, 1.0 and 1.5 m s^{-1}. The CS_1 and BC pads were tested for two velocities, 0.5 and 1.0 m s^{-1}, due to the higher pressure drop across the pads that caused water to come out of them. Small variations of the inlet air velocity through all the tests were presented. The average inlet air velocities for all the tests were similar.

Table 6. Statistical analysis of the water temperature (T_w) entering (i) and leaving (o) the pad in the wind tunnel tests. The difference between the inlet air wet-bulb temperature (T_{wb_i}) and the water temperature leaving the pad ($\Delta T_w = T_{wb_i} - T_{w_o}$) is also shown. $\overline{T}$ is the mean [°C], $\widetilde{T}$ is the median [°C], σ is the standard deviation [°C] and σ^2 is the variance [°C^2].

Pad	Entering				Leaving				$\Delta T_w = T_{wb_i} - T_{w_o}$			
	$\overline{T}_{w_i}$	$\widetilde{T}_{w_i}$	σ	σ^2	$\overline{T}_{w_o}$	$\widetilde{T}_{w_o}$	σ	σ^2	$\overline{\Delta T}_w$	$\widetilde{\Delta T}_w$	σ	σ^2
CL	20.9	20.3	1.1	1.2	19.2	19.2	0.3	0.1	0.24	0.27	0.29	0.09
CS_1	21.7	20.8	1.5	2.2	18.7	18.4	1.4	1.9	−0.24	0.18	0.72	0.09
CS_2	19.9	19.3	1.7	3.0	17.1	17.0	0.3	0.1	0.59	0.73	0.33	0.11
BC	18.5	18.0	1.4	1.8	16.3	16.3	0.2	0.5	0.91	0.91	0.22	0.05
PS_1	20.3	20.2	1.3	1.7	17.8	17.6	0.9	0.8	0.31	0.50	0.58	0.34
PS_2	21.1	21.0	0.8	0.6	19.2	19.1	0.5	0.3	0.31	0.31	0.56	0.32

Table 7. Statistics of inlet air velocity for the wind tunnel tests. $\overline{u}$ is the mean [m s^{-1}], $\tilde{u}$ is the median [m s^{-1}], σ is the standard deviation [m s^{-1}] and σ^2 is the variance [m^2 s^{-2}].

Pad	Test	$\overline{u}$	$\tilde{u}$	σ	σ^2
CL	u_1	0.554	0.570	0.041	0.002
	u_2	1.067	1.070	0.049	0.002
	u_3	1.534	1.530	0.042	0.002
	u_4	2.032	2.030	0.046	0.002
	u_5	2.534	2.540	0.053	0.003
	u_6	2.994	2.990	0.057	0.003
	u_7	3.537	3.530	0.068	0.005
CS_1	u_1	0.299	0.220	0.145	0.021
	u_2	0.888	0.840	0.091	0.008
CS_2	u_1	0.503	0.500	0.030	0.001
	u_2	1.046	1.050	0.068	0.005
	u_3	1.398	1.410	0.059	0.004
BC	u_1	0.472	0.470	0.034	0.001
	u_2	0.969	0.970	0.049	0.002
PS_1	u_1	0.507	0.510	0.030	0.001
	u_2	1.015	1.010	0.056	0.003
	u_3	1.496	1.500	0.050	0.002
PS_2	u_1	0.521	0.520	0.042	0.002
	u_2	1.002	1.000	0.048	0.002
	u_3	1.490	1.490	0.047	0.002

The porosity (ε) of the alternative pads varied between 0.44 and 0.59, which is considerably below that of the cellulose pad, which has an estimated value of 0.94. The lowest value was found for the BC pad (0.44), followed by CS_1 and PS_1 pads, both with a porosity of 0.53. The PS_2 pad had a porosity of 0.56 and the CS_2 pad had the highest porosity (0.59).

The specific surface area (ζ) was computed using the surface area per mass factor (m^2 kg^{-1}), which was obtained according to the methodology presented in Appendix A. The highest specific surface area was obtained for CS_1 (374.7 m^{-1}–0.62 m^2 kg^{-1}), similar to that for CL (372.6 m^{-1}). The BC material had a value (338.8 m^{-1}–0.34 m^2 kg^{-1}) higher than that of the CS_2 material (304.7 m^{-1}–0.56 m^2 kg^{-1}); although both materials had the same particle size, the BC had thicker particles. For the PS materials, their values were much lower: 137.6 m^{-1} (0.36 m^2 kg^{-1}) and 107.4 m^{-1} (0.30 m^2 kg^{-1}) for PS_1 and PS_2, respectively.

Table 8 shows the coefficients of Equation (3) fitted to the experimental data using the specific surface area found for each pad, and the RMSE values computed between the experimental and the predicted values of the dry-bulb temperature and the relative humidity of the outlet air, which were obtained using the mathematical model proposed by Obando et al. [32].

Table 8. Coefficients of correlation (3) used to compute the convective heat and mass transfer coefficients.

Pad	Correlation Coefficients						RMSE	
	a_1	b_1	c_1	a_2	b_2	c_2	T [°C]	ϕ [%]
CL	1.042	0.426	0.617	0.385	0.513	0.647	0.01	0.4
CS_1	0.093	0.935	1.300	0.727	0.589	0.748	0.02	0.7
CS_2	0.159	0.610	1.032	0.907	0.530	0.713	0.03	0.3
BC	0.196	0.700	0.998	0.554	0.629	0.809	0.03	0.3
PS_1	0.237	0.630	0.927	0.754	0.580	0.779	0.02	0.4
PS_2	0.186	0.890	1.064	0.689	0.641	0.864	0.01	0.3

Figure 2 shows a comparison between the predictions obtained with the mathematical model and the experimental data. For all the pads, a linear relation around the equality line (black solid line) was presented. The Wilcoxon signed rank statistical test found no statistically significant difference between the predictions and the experimental data (p-value > 0.05). ϕ_o was slightly overestimated for the alternative materials but with a bias deviation of less than 5% (dashed lines). Those results allow us to consider that the model is suitable for predicting the behaviour of the pads for other operative and constructive conditions.

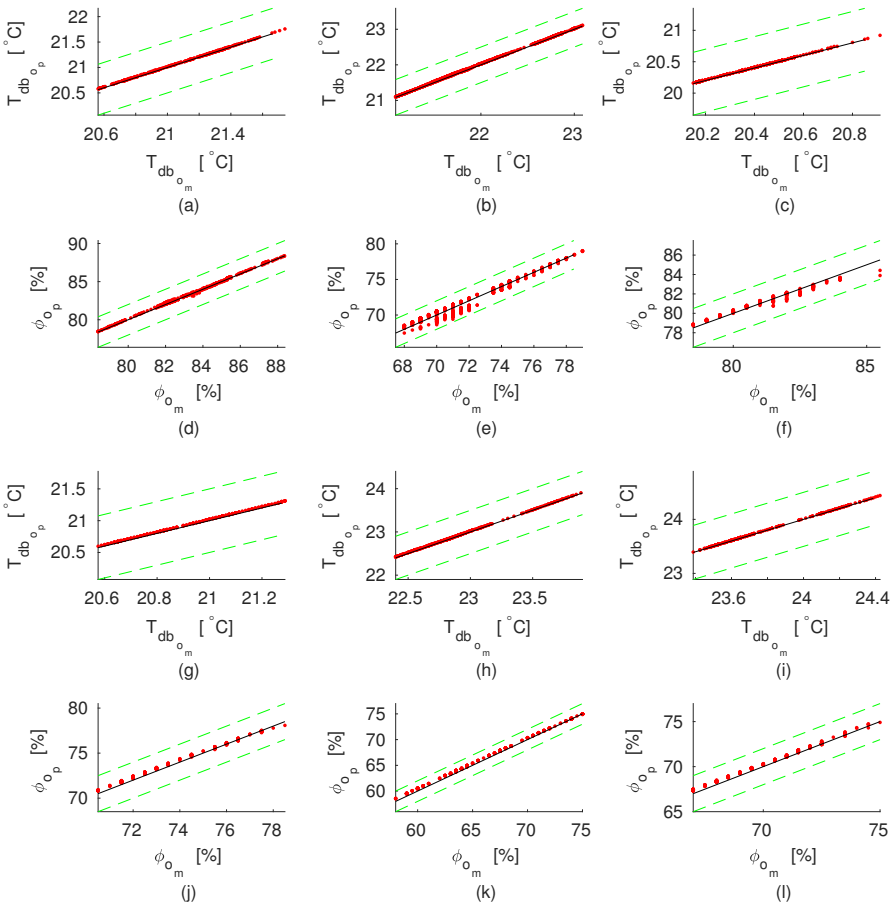

Figure 2. Comparison between the experimental data measured (m) and the model predictions (p) of the dry-bulb temperature (T_{db_o}) and relative humidity (ϕ_o) of outlet air for all the pads analysed. (**a**) T_{db_o} of CL pad. (**b**) T_{db_o} of CS_1 pad. (**c**) T_{db_o} of CS_2 pad. (**d**) ϕ_o of CL pad. (**e**) ϕ_o of CS_1 pad. (**f**) ϕ_o of CS_2 pad. (**g**) T_{db_o} of BC pad. (**h**) T_{db_o} of PS_1 pad. (**i**) T_{db_o} of PS_2 pad. (**j**) ϕ_o of BC pad. (**k**) ϕ_o of PS_1 pad. (**l**) ϕ_o of PS_2 pad. Solid black line corresponds to the equality line. Dashed lines represent the interval of ±0.5 °C and ±2% around the equality line of T_{db_o} and ϕ_o, respectively.

In Figures 3 and 4, the behaviour of the convective heat and mass transfer coefficients as functions of operative and constructive variables, such as air velocity (u), pad thickness (L), dry-bulb temperature (T_{db_i}) and relative humidity (ϕ_i) of inlet air, are shown. For this matter, the other independent variables are considered constants (u = 1.5 m s^{-1}, L = 0.1 m, T_{db_i} = 30 °C, ϕ_i = 60%).

The relationship between the convective heat transfer coefficient (h_H) and the inlet air velocity is shown in Figure 3a. A linear relationship between them is presented, corresponding to an increase in the flow of heat transferred between the air crossing the pad and the wetted pad surface when the inlet air velocity increasing. Figure 3b shows the relation between h_H and the thickness of the pad; when L decreases, h_H rises to compensate for the decrease in the wet surface area. Figure 3c,d shows that h_H remains almost constant when the dry-bulb temperature and relative humidity of inlet air change. The effect of the inlet air velocity and pad thickness change were more relevant. With the exception of the PS_2 pad, CL present the highest h_H values.

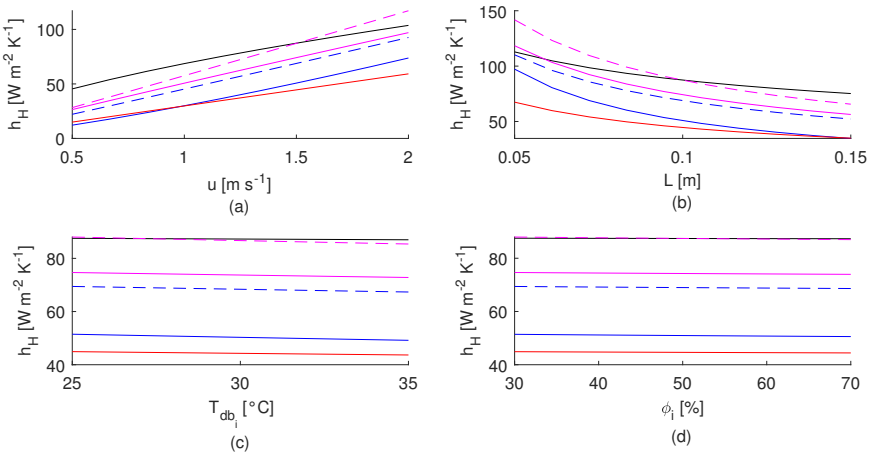

Figure 3. Comparison of the convective heat transfer coefficient (h_H) for different pad materials and their dependency of the operative and constructive variables such as air velocity (u), pad thickness (L), dry-bulb temperature (T_{db_i}) and relative humidity (ϕ_i) of inlet air. (**a**) h_H as a function of u. (**b**) h_H as a function of L. (**c**) h_H as a function of T_{db_i}. (**d**) h_H as a function of ϕ_i. For each plot the other parameters remained constants: u = 1.5 m s^{-1}, L = 0.1 m, T_{db_i} = 30 °C and ϕ_i = 60%. CL pad: black solid line, CS_1 pad: blue solid line, CS_2 pad: blue dashed line, BC pad: red solid line, PS_1 pad: magenta solid line, PS_2 pad: magenta dashed line.

The relationship between the convective mass transfer coefficient (h_M) and the inlet air velocity was shown in Figure 4a. An increase in h_H due to increasing the air velocity is presented. Thus, the evaporation rate increases according to the inlet air velocity. Figure 4b shows the relationship between h_M and the thickness of the pad. h_H also increases when the thickness of the pad decreases, to compensate for the reduction of the wet surface area. Figure 3c,d shows that h_M also remains almost constant when the dry-bulb temperature and relative humidity of inlet air change. The effect of the inlet air velocity and pad thickness changes was more significant than that caused by the dry-bulb temperature and relative humidity. In all the plots shown in Figure 4, h_H is inversely proportional to the specific surface area of each material. h_M had the lowest values for the CS pad, indicating that the amount of water evaporating from this pad is less in comparison with the others.

The surface response of η, THI, ΔT and ΔHR as functions of each pair of input variables: T_{db_i}-ϕ_i and u-L are shown in Figures A4–A11 in Appendix B. These data were obtained evaluating the model of each pad in the simulation points previously defined.

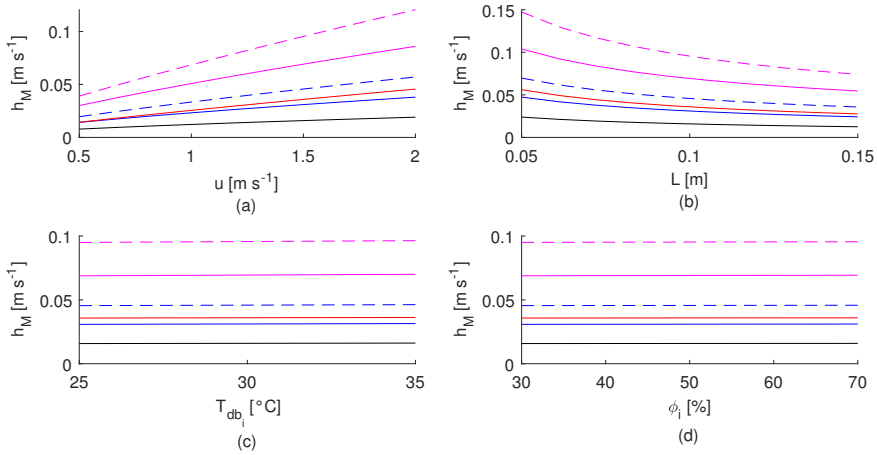

Figure 4. Comparison of the convective mass transfer coefficient (h_M) for different pad materials and their dependency of the operative and constructive variables as air velocity (u), pad thickness (L), dry-bulb temperature of inlet air (T_{db_i}) and relative humidity (ϕ_i). (**a**) h_M as a function of u. (**b**) h_M as a function of L. (**c**) h_M as a function of T_{db_i}. (**d**) h_M as a function of ϕ_i. For each plot the other parameters remained constants: u = 1.5 m s^{-1}, L = 0.1 m, T_{db_i} = 30 °C and ϕ_i = 60%. CL pad: black solid line, CS_1 pad: blue solid line, CS_2 pad: blue dashed line, BC pad: red solid line, PS_1 pad: magenta solid line, PS_2 pad: magenta dashed line.

In order to simultaneously compare all the pads, an average operating condition was analysed: u = 1.5 m s^{-1}, L = 0.1 m, T_{db_i} = 30 °C and ϕ_i = 60%. For this, one variable at a time was changed in the simulation region and each output variable was plotted separately. A detailed analysis of the behaviour of the cooling pads is presented in the following sections.

3.1. Cooling Efficiency

In Figure 5, the variation of the cooling efficiency with respect to air velocity, pad thickness, dry-bulb temperature and relative humidity of the inlet air for each pad analysed is shown. The CL pad shows the highest cooling efficiency, followed by the CS pads. The PS pads presented the lowest one. An inversely proportional correlation between the cooling efficiency and inlet air velocity for CL and PS_1 pads is shown in the Figure 5a, meanwhile a direct proportional correlation is presented for the other ones. The effect of the inlet air velocity over the cooling efficiency for the BC material was negligible. In the range of the inlet air velocity analysed, CL and CS_1 pads presented the biggest change in the cooling efficiency, up to 5.8 and 7.0%, respectively. The change was below 1.5% for the other pads. Figure 5b shown that the effect of the pad thickness over the cooling efficiency was stronger, with up to 17.4% of change for the CL pad. Figure 5c,d show the effect of the inlet air thermal conditions. All the pads show a similar behaviour, the cooling efficiency increase for high dry-bulb temperatures and low relative humidity of inlet air. The cooling efficiency was more susceptible to the changes in the relative humidity of the inlet air (ϕ_i) in comparison with the changes of the dry-bulb temperature of the inlet air (T_{db_i}). For the conditions evaluated, the cooling efficiency increased up to 1.2% (CL pad) when T_{db_i} increase, and fall up to 5.0% (CL pad) when ϕ_i augment.

No statistically significant evidence was found (p-value = 0.5114) to consider that there are differences between the medians of the PS_1 and PS_2 pads for the cooling efficiency and pad thickness relationship.

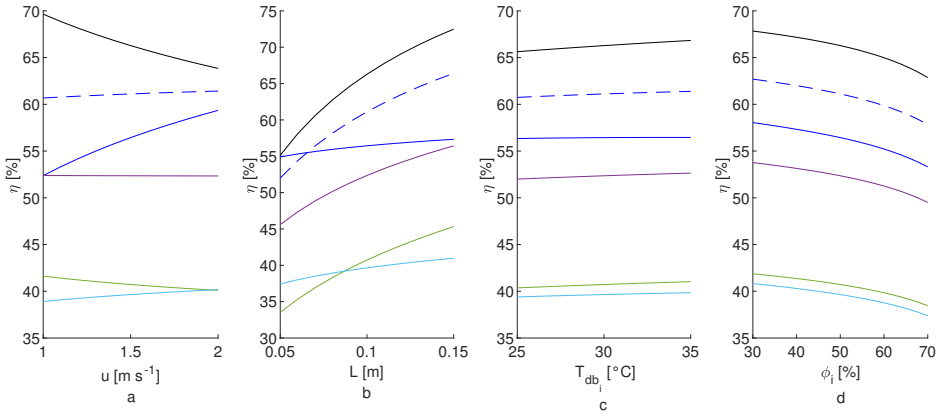

Figure 5. Comparison of pad cooling efficiency (η) of each pad analysed. (**a**) As function of inlet air velocity (u). (**b**) As function of pad thickness (L). (**c**) As function of dry-bulb temperature of inlet air (T_{db_i}). (**d**) As function of relative humidity of inlet air (ϕ_i). For each plot the other parameters remained constants: u = 1.5 m s^{-1}, L = 0.1 m, T_{db_i} = 30 °C and ϕ_i = 60%. CL: solid black line; CS_1: blue solid line; CS_2: blue dashed line; BC: red solid line; PS_1: magenta solid line; PS_2: magenta dashed line.

3.2. Temperature–Humidity Index

Figure 6 shows the behaviour of the Temperature–Humidity Index computed for the outlet pad thermal conditions. THI computed for the external thermal conditions was also shown for comparison purposes (green dash-doted line). THI at pads outlet was below the THI at pad inlet, thus all the pads improved the thermal comfort conditions of the air at outlet. As a reference, the zone of the middle thermal stress defined for cattle is shown with black dash-dot lines ($72 \leq THI \leq 78$) [55]. For the inlet thermal conditions analysed (T_{db_i} = 30 °C and ϕ_i = 60%), Figure 6a,b shows that the THI of the CL pad was furthest away, around 5.5 units below the external THI, followed by the CS pads (around 4.1 units below). The PS pads were closer to the external THI (around 2.6 units below). The inlet air velocity and pad thickness changes have little effect over THI. Figure 6a shows that the THI behaviour of the CL pad varied inversely to the alternative pads, which decrease THI when increasing the inlet air velocity. It is not possible to generalize the behaviour due to the pad thickness influence, because for the CS_1 and PS_2 pads it was opposite to the CL pad's behaviour, as is shown in Figure 6b. Due to the way THI was computed, the dry-bulb temperature and relative humidity of inlet air have a strong influence over it. When T_{db_i} changed, the THI upper limit of the middle comfort zone (THI = 78) in Figure 6c was reached before by the PS_2 pad at 30.7 °C and 1.7 °C above it by the CL pad. THI increased linearly with T_{db_i} with the same slope for all the pads (≈1.4 THI units per T_{db_i} unit). A similar behaviour occurs when ϕ_i changed. THI was less susceptible to ϕ_i changes than to T_{db_i} ones (≈0.3 THI units per ϕ_i unit for the CL pad). The upper limit of the middle thermal comfort zone (THI = 78) is reached before by the PS_2 pad when ϕ_i was 54.8% and later by the CL pad when ϕ_i was 63.9%.

Non statistically significant evidence was found ($0.3246 \leq p$-value ≤ 0.7427) to consider that there are differences between the medians of all the pads for the THI and dry-bulb temperature of the inlet air relationship, between the medians of all the pads (except between CL and PS pads) for the THI and relative humidity of the inlet air relationship ($0.1020 \leq p$-value ≤ 0.8014).

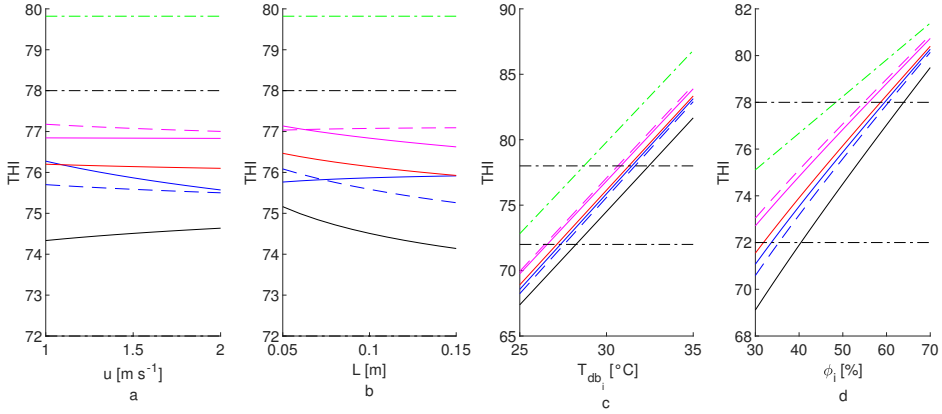

Figure 6. Comparison of the air outlet Temperature–Humidity Index (THI) of each pad material analysed. (**a**) As function of inlet air velocity (u). (**b**) As a function of pad thickness (L). (**c**) As a function of dry-bulb temperature of inlet air (T_{db_i}). (**d**) As a function of relative humidity of inlet air (ϕ_i). For each plot, the other parameters remained constant: u = 1.5 m s^{-1}, L = 0.1 m, T_{db_i} = 30 °C and ϕ_i = 60%. CL: solid black line; CS_1: blue solid line; CS_2: blue dashed line; BC: red solid line; PS_1: magenta solid line; PS_2: magenta dashed line; inlet air THI: green dash-dot line; middle thermal comfort THI zone for cattle: black dash-dot line.

3.3. Air Dry-Bulb Temperature Drop

As is shown in Figure 7, ΔT was highest for the CL pad and lowest for the PS pads. For low inlet air velocity ΔT was highest for CL and CS_2 pads, as is shown in Figure 7a. There is no generalized behaviour of ΔT as a function of u, with CL and PS_1 presented a direct correlation but inverse for the other pads. However, the influence of the inlet air velocity over ΔT could be neglected since a change of 1 m s^{-1} increased ΔT up to 0.5 °C for the CS_1 pad; for the other pads ΔT was lower. On the other hand, changes in the pad thickness (Figure 7b), dry-bulb temperature (Figure 7c) and relative humidity of the inlet air (Figure 7c) have a greater impact on ΔT. Increasing the thickness of the pad increases ΔT in 1.3 °C for the CL pad; for the other pads ΔT also increases in a lower range. ΔT changed linearly with the dry-bulb temperature and relative humidity of the inlet air, being more susceptible to the changes of relative humidity. When T_{db_i} rises, ΔT increases 1.0 °C and 0.6 °C for the CL and PS_2 pads, respectively, which correspond to an increment of 0.1 °C and 0.06 °C per unit of Ti change. When ϕ_i increase, ΔT decrease 5.1 °C and 3.1 °C for the CL and PS_2 pads, respectively, that correspond to a decrease of 0.13 °C and 0.08 °C per unit of ϕ_i change.

Non statistically significant evidence was found to consider that there are differences between the medians of PS_1 and PS_2 pads for the dry-bulb temperature drop relationship with the pad thickness (p-value = 0.5114) and inlet air dry-bulb temperature (p = 0.3246); between the medians of pads $CL - CS_1$, $CL - CS_2$, $CS - BC$, $CS_1 - CS_2$ and $PS_1 - PS_2$ for the dry-bulb temperature drop and relative humidity of the inlet air relationship ($0.1249 \leq p$-value ≤ 0.8014).

3.4. Relative Humidity Increase

Contrary to the results presented before, the increase of the relative humidity at the outlet of the pads ($\Delta\phi$) for the CL pad was located between the alternative pad's results, as is shown in Figure 8. The lowest $\Delta\phi$ was for the PS pads, followed by the CL pad, while the CS_2 had the highest. $\Delta\phi$ of the CS_1 pad increased when the inlet air velocity increasing; opposite to the behaviour of the other alternative pads (Figure 8a). The CL pad presented the highest change of $\Delta\phi$ (3.8%) due to inlet air velocity. The influence of the pad thickness over $\Delta\phi$ is stronger, changing up to 10.0% for the CL pad (Figure 8b). $\Delta\phi$ increases when increasing the pad thickness, for all the pads. Increasing the dry-bulb temperature of inlet air had a non-significant effect on $\Delta\phi$, with a maximum change of 1.2% for the PS_2 pad (Figure 8c). In this case, the behaviour of the CL pad was opposite to

the alternative pads, indicating that the CL pad increase the evaporation rate when T_{db_i} increased. $\Delta\phi$ across the pads was more susceptible to the changes in the relative humidity of inlet air. Figure 8d shows that all the pads present the same behaviour, decreasing $\Delta\phi$ when increasing ϕ_i. The changes of $\Delta\phi$ were between 22.3% and 13.4% for the CS_2 and PS_1 pads, respectively. Those values correspond to a decrease of 0.6% and 0.3% per unit increment of ϕ_i, respectively. When ϕ_i increased, decrease the ability of the air to hold the water vapour and consequently evaporate a less amount of water from the pads.

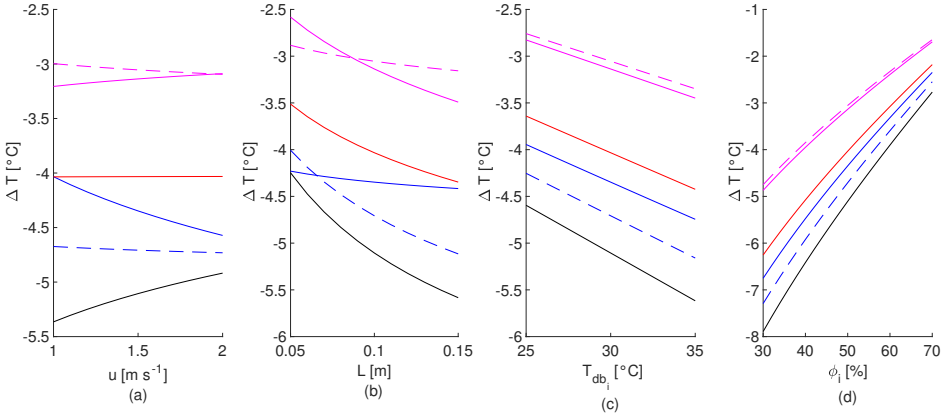

Figure 7. Comparison of inlet-outlet air dry-bulb temperature change (ΔT) of each pad material analysed. (**a**) As function of inlet air velocity (u). (**b**) As function of pad thickness (L). (**c**) As function of dry-bulb temperature of inlet air (T_{db_i}). (**d**) As function of relative humidity of inlet air (ϕ_i). For each plot the other parameters remained constants: u = 1.5 m s^{-1}, L = 0.1 m, T_{db_i} = 30 °C and ϕ_i = 60%. CL: solid black line; CS_1: blue solid line; CS_2: blue dashed line; BC: red solid line; PS_1: magenta solid line; PS_2: magenta dashed line.

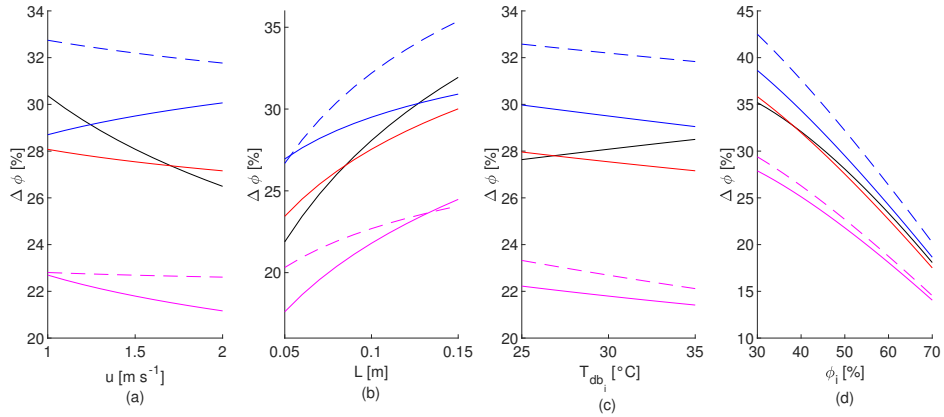

Figure 8. Comparison of inlet-outlet relative air humidity change ($\Delta\phi$ [%]) of each pad material analysed as a function of operative and geometric parameters. (**a**) As function of inlet air velocity (u). (**b**) As function of pad thickness (L). (**c**) As function of dry-bulb temperature of inlet air (T_{db_i}). (**d**) As function of relative humidity of inlet air (ϕ_i). For each plot the other parameters remained constants: u = 1.5 m s^{-1}, L = 0.1 m, T_{db_i} = 30 °C and ϕ_i = 60%. CL: solid black line; CS_1: blue solid line; CS_2: blue dashed line; BC: red solid line; PS_1: magenta solid line; PS_2: magenta dashed line.

Non statistically significant evidence was found to consider that there are differences between the medians of CL and BC pads for the relative humidity increment and inlet air velocity relationship (p-value = 0.2934); between the medians of the paired pads $CL - CS_1$, $CL - BC$, $CS_1 - CS_2$ and $PS_1 - PS_2$ for the relative humidity increment and the pad thickness relationship ($0.2934 \leq p$-value ≤ 0.6936); and between the medians of the pads $CL - CS_1$, $CL - BC$, $CS_1 - CS_2$, $CS_1 - BC$ and $PS_1 - PS_2$ for the relative humidity increment and the relative humidity of inlet air relationship ($0.2085 \leq p$-value ≤ 0.8999).

Table 9 shows a comparison between the output pad variables: η, THI, ΔT and $\Delta\phi$ for constant input variables: u = 1.5 m s^{-1}, L = 0.1 m, T_{db_i} = 30 °C and ϕ_i = 50%. For this conditions, the CS pads present the best behaviour between the alternative pads: highest cooling efficiency, lowest THI, highest dry-bulb temperature drop but also the highest relative air humidity increasing. The lowest ΔT of the PS pads do not compensate the increasing of ϕ, obtaining the highest values of THI.

Table 9. Cooling efficiency (η), Temperature–Humidity Index (THI), dry-bulb temperature drop (ΔT) and relative humidity increment ($\Delta\phi$) for average input variables: inlet air velocity (u = 1.5 m s^{-1}), pad thickness (L = 0.1 m), dry-bulb temperature (T_{db_i} = 30 °C) and relative humidity of inlet air (ϕ_i = 50%). $\Delta\eta$ is the difference between η of the alternative pads and the CL pad. ΔTHI is the difference between the THI compute with the outlet and inlet (79.8) air thermal conditions.

Pad	η ($\Delta\eta$) [%]	THI (ΔTHI)	ΔT [°C]	$\Delta\phi$ [%]
CL	66.3	74.5 (5.3)	−5.1	28.1
CS_1	56.4 (−9.9)	75.9 (3.9)	−4.3	29.5
CS_2	61.1 (−5.2)	75.6 (4.2)	−4.7	32.2
BC	52.4 (−13.9)	76.1 (3.7)	−4.0	27.5
PS_1	40.7 (−25.6)	76.8 (3.0)	−3.1	21.8
PS_2	39.6 (−26.7)	77.1 (2.7)	−3.0	22.7

3.5. Pressure Drop across the Pad

Table 10 summarized the statistical description of the pressure drop measured across the pads (ΔP). Larger differences of the average values of ΔP between the cellulose and the alternative pads were evident. Even at high speeds ($u_7 \approx$ 3.5 m s^{-1}), the cellulose ΔP is around the obtained for the air velocity tested in the other materials (for $u \leq$ 1 m s^{-1}). The variability of the measured ΔP also shows big differences. This is mainly due to an increase in resistance to air flow caused by increasing water flow through the pads. For each air velocity, up to three water flows were evaluated. The low variability of the CS_2 material for the inlet air velocity u_3 was because, in this test, only the lowest flow of water was evaluated; when water flow was increased, liquid water came out of the pads. The PS pads present the lowest variability from the alternative pads, indicating that water flow does not considerably affect the air flow resistance in them.

Table 10. Statistics of pressure drop across the cooling pad (ΔP) for the wind tunnel tests. $\overline{\Delta P}$ is the mean [Pa], $\widetilde{\Delta P}$ is the median [Pa], σ is the standard deviation [Pa] and σ^2 is the variance [Pa^2].

Pad	Test	$\overline{\Delta P}$	$\widetilde{\Delta P}$	σ	σ^2
CL	u_1	1.2606	1.2700	0.0955	0.0091
	u_2	3.5558	3.6100	0.2227	0.0496
	u_3	6.9345	6.9500	0.2199	0.0484
	u_4	12.3764	12.3800	0.3067	0.0941
	u_5	18.2361	18.2700	0.4733	0.2240
	u_6	24.0571	24.2300	0.5083	0.2584
	u_7	31.5677	31.8500	0.9008	0.8114
CS_1	u_1	20.7298	10.5400	20.3817	415.4150
	u_2	109.3886	115.4700	22.1462	490.4554
CS_2	u_1	22.2006	21.0000	2.7782	7.7182
	u_2	89.9411	78.3650	19.5662	382.8370
	u_3	133.2440	132.3500	3.7064	13.7374
BC	u_1	33.6239	30.7100	8.5841	73.6868
	u_2	134.8465	131.6900	24.7958	614.8340

Table 10. *Cont.*

Pad	Test	$\overline{\Delta P}$	$\widetilde{\Delta P}$	σ	σ^2
PS_1	u_1	17.6566	17.7000	1.2807	1.6401
	u_2	60.6392	61.8000	6.4748	41.9233
	u_3	116.5752	112.2400	7.9055	62.4964
PS_2	u_1	12.8821	12.7850	1.2633	1.5959
	u_2	40.8870	41.4500	2.7954	7.8142
	u_3	87.5552	88.1300	4.6572	21.6894

The average values of water flow presented in Table 11 were around 2, 6.2 and 10 L min^{-1} m^{-1} values as defined before. The variability of the water flow measurements was below 0.7 L min^{-1} m^{-1}, being considerably lowest for the cellulose pad tests.

Table 11. Statistics of water flow for all tests in the wind tunnel. $\overline{Q}$ is the mean [L min^{-1} m^{-1}], $\tilde{Q}$ is the median [L min^{-1} m^{-1}], σ is the standard deviation [L min^{-1} m^{-1}] and σ^2 is the variance [L^2 min^{-2} m^{-2}].

Pad	Test	$\overline{Q}$	$\tilde{Q}$	σ	σ^2
CL	Q_1	1.9450	1.9400	0.0414	0.0017
	Q_2	6.1400	6.1200	0.0573	0.0033
	Q_3	10.0170	10.0400	0.0440	0.0019
CS_1	Q_1	1.9827	1.9400	0.0852	0.0073
	Q_2	6.1321	6.1200	0.1640	0.0269
	Q_3	8.1764	8.1300	0.4248	0.1805
CS_2	Q_1	1.9896	1.9800	0.1389	0.0193
	Q_2	5.9684	6.0400	0.2677	0.0716
	Q_3	9.7014	9.7600	0.5464	0.2986
BC	Q_1	2.0832	2.0500	0.2869	0.0823
	Q_2	6.0147	5.9800	0.2579	0.0665
	Q_3	9.7360	9.7900	0.4150	0.1723
PS_1	Q_1	2.3979	2.4400	0.2310	0.0534
	Q_2	6.0732	6.0800	0.7191	0.5171
	Q_3	8.6864	8.6600	0.6682	0.4465
PS_2	Q_1	2.1481	2.1600	0.2472	0.0611
	Q_2	6.3353	6.2200	0.6723	0.4520
	Q_3	8.6104	8.4800	0.6734	0.4535

Average pressure drop across the cellulose pad varied from 1.2 Pa when u = 0.5 m s^{-1} and Q = 2 L min^{-1} m^{-1} to 32.3 Pa when u = 3.5 m s^{-1} and Q = 10 L min^{-1} m^{-1}. While the pad with PS_2 material was above 10 Pa and the other ones were above 20 Pa for the minimum speed tested. This shows a big difference between ΔP of the cellulose and the alternative materials. Figure 9 shows the ΔP for an inlet air velocity of 1.0 m s^{-1} and a water flow of 6.2 L min^{-1} m^{-1}. The CS_1 presents the highest ΔP due to the used of the smallest particle size, while the PS pads present the lowest ΔP, between the alternative pads. The PS_2 had the lowest value due to the highest particle size. The differences in the ΔP values were more noticeable for high u and Q values (data not show).

Figure 10 shows the normalized average pressure drop across the different pads tested as a function of the inlet air velocity with a constant water flow of 6.2 L min^{-1} m^{-1}. As was expected for a porous medium, ΔP increased with u. When ΔP was normalized with respect to the maximum ΔP of each pad material, no visual differences in the behaviour of ΔP as u changed were seen. From low to high u, ΔP was affected in the same way for all the pads. The relation between ΔP and u can be described with the same exponential function, fitted to their respectively ΔP values for each pad material.

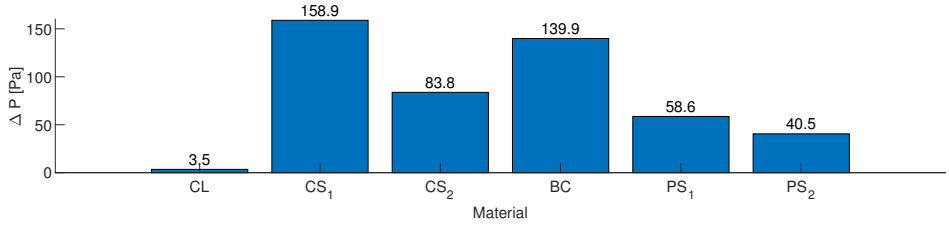

Figure 9. Pressure drop across the pads studied for a fixed value of inlet air velocity (u = 1 m s^{-1}) and water flow (Q = 6.2 L min^{-1} m^{-1}).

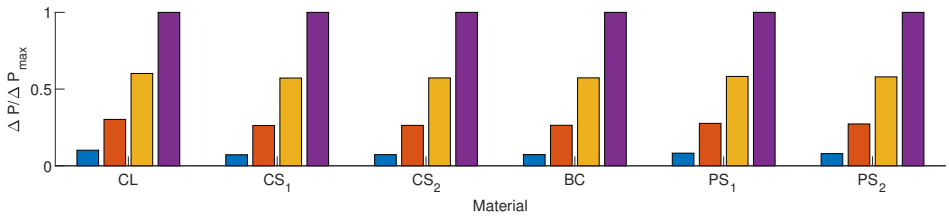

Figure 10. Normalized pressure drop as a function of inlet air velocity (u) for a constant water flow of 6.2 L min^{-1} m^{-1}. The colour bars corresponds to different air velocities: blue: u = 0.5 m s^{-1}, red: u = 1.0 m s^{-1}, orange: u = 1.5 m s^{-1} and magenta: u = 2 m s^{-1}.

Figure 11 shows the normalized average pressure drop across the different pads tested as a function of the water flows for a constant inlet air velocity of 1 m s^{-1}. For all the pads, except for the cellulose one, the pressure drop is highly influenced by the water flow through the pad, being the CS_1 pad the most affected and the PS pad the least affected. The ΔP of the cellulose pad changes about 9% due to increasing the water flow, meanwhile the CS_1 pad changes 80%. In the cellulose material, the water forms a thinner layer in comparison with the alternative pads where it considerably increases the resistance to air flow.

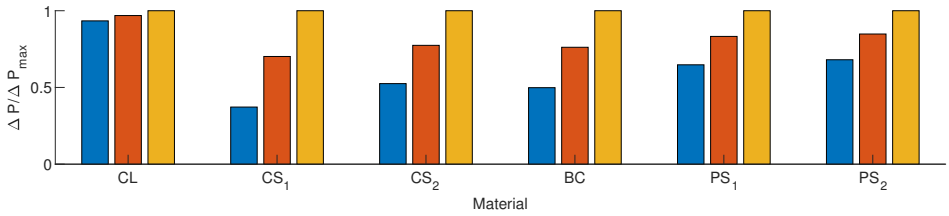

Figure 11. Normalized pressure drop as a function of water flow for an air velocity of 1 m s^{-1}. The colour bars correspond to different water flows: blue: Q = 2 L min^{-1} m^{-1}, red: Q = 6.2 L min^{-1} m^{-1} and orange: Q = 10 L min^{-1} m^{-1}.

3.6. Permeability

Equation (5) adequately reproduces the relationship between the pressure drop across the pad and inlet air velocity, as is shown in Figure 12 for the BC pad. In this case, the permeability (K) and the Forchheimer coefficient (β) of the equation were estimated for each water flow used.

To obtain a universal expression to compute the pressure drop across the pad as a function of the inlet air velocity and the water flow, the permeability and the Forchheimer coefficient were considered proportional to water flow, as $K(Q) = \frac{1}{f_1+f_2Q}$ and $\beta(Q) = (g_1 + g_2Q)$. Two additional cases were evaluated: assuming that the permeability was water flow dependent or that the Forchheimer coefficient was water flow dependent.

The goodness of the fitted equations was compared through the coefficient of determination (R^2) and the RMSE. The best values were obtained when the permeability was considered constant and the Forchheimer coefficient as a function of the water flow. Figure 13 compares Equation (5) fitted to each water flow when the permeability and the Forchheimer coefficient were considered as constants (solid line), and fitted to all the

experimental data (asterisk markers), considering the permeability as a constant and the Forchheimer coefficient as a function of the water flow. There was no visible difference between them for $u < 1.0$ and a slight deviation for higher u was detected. Table 12 summarizes the g's coefficients, R^2, RMSE, permeability and the Forchheimer coefficient for a water flow of 6.2 L min^{-1} m^{-1} for comparison purposes.

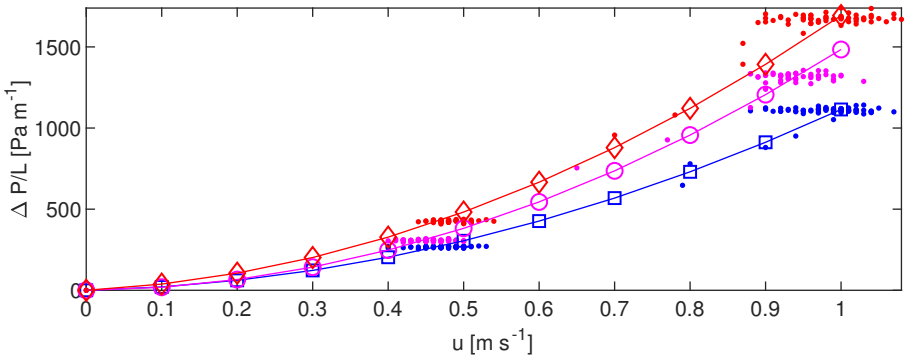

Figure 12. Darcy-Forchheimer Equation (5) fitted to the experimental data of pressure drop (ΔP) and inlet air velocity (u) for different water flows (Q) for the *BC* material. Blue: 2 L min^{-1} m^{-1}, magenta: 6.2 L min^{-1} m^{-1} and red: 10 L min^{-1} m^{-1}.

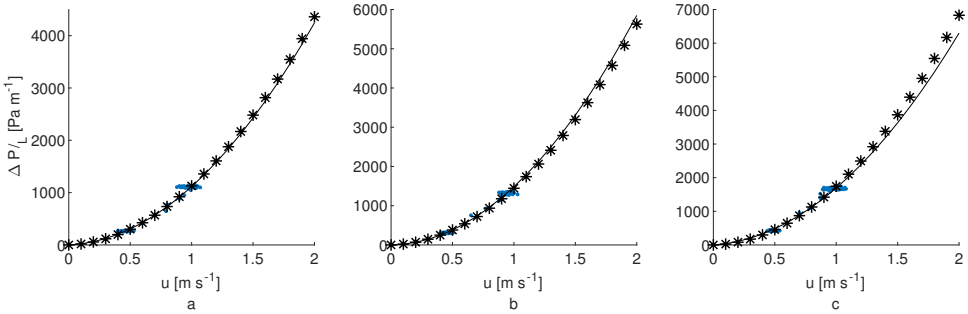

Figure 13. Comparison of the *BC* pad experimental pressure drop (blue point) computed with the Darcy–Forchheimer Equation (5) considering the permeability and Forchheimer as a constant and the equation fitted for each water flow (black solid line) and considering the permeability constant and the Forchheimer coefficient as a function of the water flow (asterisk markers). (**a**) Water flow of 3.1 L min^{-1} m^{-1}. (**b**) Water flow of 6.2 L min^{-1} m^{-1}. (**c**) Water flow of 10.0 L min^{-1} m^{-1}.

Table 12. Permeability (K) and coefficients used to compute the Forchheimer coefficient as a function of water flow ($\beta(Q) = (g_1 + g_2 Q)$) in Equation (5). The coefficient of determination (R^2) and the Root Mean Square Error (RMSE [Pa]) of the fitted equation are presented. The Forchheimer coefficient for a water flow of 6.2 L min^{-1} m^{-1} for comparison purposes is also shown.

Pad	g_1	g_2	R^2	RMSE [Pa]	K [m^2]	β(6.2) [m^{-1}]
CL	20.8546	0.2351	0.9997	0.18166	1.3959×10^{-6}	22.31
CS_1	946.7572	72.6893	0.9988	1.36296	1.0108×10^{-7}	1397.4
CS_2	551.5387	39.3833	0.9995	1.05007	3.6648×10^{-7}	795.7
BC	891.2264	82.1001	0.9991	1.63633	2.4308×10^{-7}	1400.2
PS_1	358.6404	17.9078	0.9995	0.90228	1.4939×10^{-7}	469.7
PS_2	287.9664	9.8696	0.9993	0.85144	2.6975×10^{-7}	349.2

As the pad is constantly wetted, the water forms a thick layer over the material, which affects the flow of air, increasing ΔP. However, the permeability could be considered constant, while the Forchheimer coefficient changes with the water flow. The coefficient g_2 shows the effect of the water flow over ΔP. For the cellulose material, this parameter is small. For the CS_1 and BC materials this parameter presents significant influence as was shown previously in Figure 11.

The permeability of the alternative materials were ten times lower than that of the cellulose material, which is in the order of 1×10^{-6}. It was not possible to establish a correlation between the permeability and the magnitude of ΔP across the alternative pads. However, this relation is clearly established with the Forchheimer coefficient. This was biggest for CS_1 and BC pads, which are the ones that produce the highest ΔP, while the lowest $\beta(6.2)$ values were obtained for the PS pads, which produces the least ΔP.

Additionally, there was a big difference between the Forchheimer coefficient of the cellulose and the alternative pads. The Forchheimer coefficient can be considered an indicator of how big the ΔP changes are when the inlet air velocity increases. The alternative pads with the biggest particle size (PS) present the lowest Forchheimer coefficients, while the CS_1 pad, which has the smallest particle size, and the BC materials, which have the least porosity, present the maximum values; the effect of the inlet air velocity over ΔP is stronger. When the water flow increases, an increase in the resistance to the air flow was also more noticeable on those pads.

4. Discussion

The experimental results showed that the pads evaluated produced cooling efficiencies above 42% and temperature drops up to 5.0 °C, as can be seen in Figures 5 and 7, even with environmental conditions that are not suitable for evaporative cooling (low dry-bulb temperature and high relative humidity of inlet air). The major drawback is the increase in relative humidity that in this case was up to 35%.

The alternative pads presented similar results to those of the cellulose pads. However, the environmental conditions were not kept constant due to experimental limitations, making it difficult to established an unbiased comparison between the pads from the experimental test results. For this reason, the model proposed by Obando et al. [32] was used to simulate each one of the pads in equal environmental and operative conditions. The results presented in Table 8 and Figure 2 show that the model used adequately describes the behaviour of each pad. With this, it was indeed possible to obtain the correlation (3) to compute the convective heat and mass transfer coefficients of each pad, which is useful for performing different thermo-fluid analysis as in Computer Fluid Dynamics simulations. There are few research studies about cooling pads that report those coefficients, ref. [13] being the first one to report the coefficients of the coconut coir fibre and non-woven fabric perforated materials. This study allowed us to confirm that the cellulose pad coefficients were similar to those found by Dhamneya et al. [5], Kulkarni and Rajput [21], Laknizi et al. [30], Franco et al. [56], Chen et al. [57]. The cellulose pad studied in this work serves as reference to validate the model proposed by Obando et al. [32].

Several research studies are in concordance with the inverse correlation of the cooling efficiency and the relative humidity with the air inlet velocity found here [1,24,29]. Although the behaviour of the coconut shield with small particles (CS_1) was unexpected, some other research studies had documented similar behaviours [12,13,58] with pads based on natural fibres. This behaviour could be attributed to the resistance to the air flow across the pad. For some pads, especially with smaller particle sizes, such as the CS_1 pad, the particles are arranged in such a way that the high resistance to air flow limits the free transit of the air across the pad, decreasing the surface area in contact with the water. When the inlet air increases, the pressure drop forces the air to flow through small orifices that could be full of water, raising the turbulence of the flow, incrementing the water–air contact and resulting in a drastic decrease in the dry-bulb temperature of outlet air. For the other material that had a lower particle size, the effect is less noticeable.

According to the results shown in Figures 3 and 4, the magnitude of the convective heat and mass transfer coefficients are inversely proportional to the specific surface area found for the alternative pads. That is, those coefficients compensate in some way for the low magnitude of the total wetted surface. On the other hand, alternative pads that had a similar specific surface area to the cellulose one (coconut shells and burnt clay brick) presented the highest cooling efficiency, with a high relative humidity at the outlet, which

is also an indicator of high water consumption, while the cellulose pad kept it lower due to its lower convective mass transfer coefficient.

The accuracy of the model results was not affected by not considering the water flow in accordance with [27–29,44] or the porosity of the materials as was established by Osorio et al. [16]. It was considered that the water flow was enough to maintain the pads wetted. Water flow beyond the maximum evaporation rate has no beneficial effects [31], and it only affects the pressure drop across the pad, as was shown in Figure 11. So, it is desirable to maintain an equilibrium between the water flow and the evaporative water rate. Similar results were reported by Liao and Chiu [26], Franco et al. [31].

There was a difference above 90% between permeability of the cellulose and the alternative pads, as was reflected in the high pressure drop across these, especially for pads with small particle sizes. Similar pressure drops for alternative materials were reported by Jain and Hindoliya [7], Vijaykumar et al. [14], Basiouny and Abdallah [23], Liao and Chiu [26], Kovács et al. [59].

Based on the Darcy–Forchheimer Equation (5), it was possible to obtain a universal expression for each of the pads analysed to compute the pressure drop in terms of the inlet air velocity and the water flow. Additionally, it was determined that the permeability was not affected by the water flow as it was for the Forchheimer coefficient. Attempts to obtain an expression that describes the relation between inlet air velocity and water flow were made previously by [28,36], adding the characteristic length (l_e) without including viscous or inertial force coefficients such as the permeability and the Forchheimer coefficients.

The high pressure drop across the alternative small particle pads made them unfeasible for some applications, even with their high cooling efficiency, because higher exhaust fans are required, increasing the electrical power consumption. Nevertheless, other alternative materials, such as the pumice stones, could be used in applications where a continuous ventilation system with low heat load is required. Those pads could decrease the external temperature by up to 2.0 °C maintaining a low pressure drop and a low increase in relative humidity.

The pad cooling efficiency is one of the main parameters that had been used to characterize the effectiveness of an evaporative cooling system. However, the use of other quantities made its applicability or benefits to the end user clearer, such as to farmers in agro-industrial facilities. The drop in temperature and the increase in relative humidity in the air leaving the pad provides a clearer idea of the improvement in the thermal conditions of the air. The influence of both variables on the thermal comfort of animals can also be combined in a unique index such as the THI, which gives a better idea of the cooling effect of the thermal comfort of animals inside the facilities, being one of the goals of air conditioning.

The relationship found between the THI, the inlet air velocity and the pad thickness for the cellulose pad were in agreement with the results found previously by Sayed and Khater [39]. Indeed, it was found that, with any of the pads evaluated, it was possible to improve the external thermal conditions of the air maintaining inside the installation a middle thermal comfort zone defined for cattle, up to $T_{db_i} = 30$ °C (worst pad behaviour with $\phi_i = 60\%$). If the input relative humidity decreases, it could increase the temperature limit. So, any of the pads could be used to improve the thermal conditions of the air.

When an evaporative system is implemented, it was evident from the results that thicker pads provided higher cooling efficiency. However, this improved with an increasing in the evaporative water rate. When it is going to be used in tropical and subtropical countries such as Colombia, where high relative humidity was predominant, this result is not desirable. So, for these climatic conditions, it is recommended to use pads of 0.1 m of thickness, providing a balance between the dry-bulb temperature drop and the increase in the relative humidity.

5. Conclusions

Using a mathematical model fitted to wind tunnel experimental data, it was possible to perform a complete characterization of several evaporative cooling pads, manufac-

tured with cellulose and alternative materials, in terms of cooling efficiency, Temperature–Humidity Index, dry-bulb temperature drop, relative humidity increment and pressure drop across the pads; as functions of the inlet air velocity, water flow and pad thickness. Pad efficiencies were found between 40% and 70% for pads manufactured with alternative materials for inlet air environmental conditions typical of tropical climate countries like Colombia. The alternative pads with lower particle sizes (higher specific surface area) present cooling efficiencies similar to the cellulose pads (70%) at the expense of a higher pressure drop.

All pads evaluated can improve the inlet air thermal conditions, providing outlet air with Temperature–Humidity Indices below the external environmental conditions and maintaining the mean thermal comfort zone for a broad range of dry-bulb temperatures and relative humidity combinations, making them useful for several applications.

The methodology presented here allows the characterization of new alternative materials in order to find those that provide an adequate balance between cooling efficiency and pressure drop across the pad. Additionally, new simulations can be performed using the convective heat and mass transfer coefficients correlations found for particular conditions.

To decrease the pressure drop across the pads and consequently the electrical power consumption, it is necessary to set the water flow to the minimum value required to maintain the wetted pad, which depends on the evaporation rate, especially when high speeds (above 1.5 m s^{-1}) are used.

Author Contributions: Conceptualization: F.A.O.V. and J.A.O.S.; data acquisition: F.A.O.V.; data analysis: F.A.O.V. and A.P.M.R.; design of methodology: F.A.O.V. and J.A.O.S.; writing and editing: F.A.O.V., A.P.M.R., J.A.O.S., F.A.D. and M.B. All authors have read and agreed to the published version of the manuscript.

Funding: This research received no external funding.

Institutional Review Board Statement: Not applicable.

Informed Consent Statement: Not applicable.

Data Availability Statement: The data presented in this study are available on request from the corresponding author.

Conflicts of Interest: The authors declare no conflict of interest.

Appendix A. Image Processing for Compute Specific Surface Area

Appendix A.1. Coconut Shells and Burnt-Clay Hollow Bricks Particles

Several photographs of particles samples of coconut shells and burn clay bricks were taken using a template of 34.5 cm^2 of black area (Figure A1). Photographs were binarized (Figure A2) using the toolbox of image processing of MATLAB® [60]. A relation between the surface area and the weight of each sample were obtained using the following procedure: for each photography, the number of black pixels of the black template were computed, obtaining the number of pixel per cm^2, with this, the surface area of one side of particles were estimated. The specific surface area of particles is obtained multiplying this value by 2 and divided it for the weight of sample.

The surface area per volume unit (specific surface area, ζ) of the pad results when the obtained specific surface area is multiply by the bulk density of the material (weight of the material used to filled the pad over the volume of the pad). For the burnt-clay hollow bricks particles, the perimeter of each particle were compute and multiply for the mean thickness of the particles (1.2 cm) to obtain the surface area lateral sides. This value was added to the area of sample computed before. Table A1 summarized the data results from image processing for both materials.

Table A1. Average data obtained through image processing of photographs samples. 32.5 cm^2 was the black area of template used.

	Coconut Shells		Burn Clay Brick
Particle size	7.9–12.7 mm	12.7–19.0 mm	12.7–19.0 mm
Number of pixels for template	403,980	391,481	393,551
Pixel per area unit [px cm^{-2}]	11,710	11,347	11,407
Pixels per sample	2,679,380	2,289,517	1,751,209
Area of sample [cm^2]	457.9848	405.6077	583.5528
Weight of sample [g]	73.625	72.125	170.87
Surface area per mass unit [m^2 kg^{-1}]	0.6221	0.5617	0.3415
Weight of material of pad [kg]	16.6	14.95	30
Pad volume [m^3]	0.02756	0.02756	0.03024
Specific surface area of pad [m^{-1}]	374.70	304.69	338.78

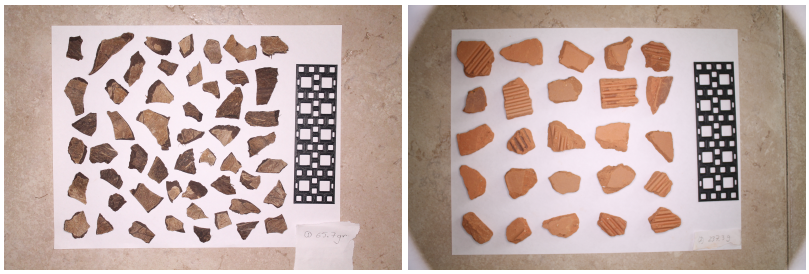

(**a**) (**b**)

Figure A1. Photographs of material samples to compute the specific surface area through image processing. (**a**) Particles of coconut shells. (**b**) Particles of burn clay bricks.

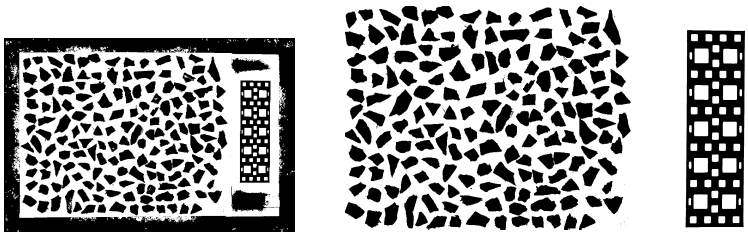

(**a**) (**b**) (**c**)

Figure A2. Image processing to compute the surface area of coconut and burn clay particles. (**a**) Binarized image. (**b**) Image extracted from particle sample. (**c**) Image extracted from template.

Appendix A.2. Pumice Stones

Two equations to estimate the surface area were (S) compared, Knud Thomsen Formulae (A1) and Dall Equation (A2) [48]. These equations approximate the geometry of a stone to a spheroid shape.

$$S = 4\pi\left(\frac{(lw)^{1.6075} + (lh)^{1.6075} + (wh)^{1.6075}}{3}\right)^{\frac{1}{1.6075}} \quad \text{(A1)}$$

$$S = \frac{\pi}{3}(lw + lh + wh) \quad \text{(A2)}$$

where l, w and h are the length, width and height of the stone.

To select the best way to compute the surface area, a sample of 16 pumice stones of size 34.9–45.0 mm were randomly select. Each particle was cover with a single layer of aluminium foil (Figure A3a). The aluminium foil was then spread over a black background (Figure A3b) and photographs altogether with a template of 34.5 cm^2 of black area were taken to compute the surface area through image analysis. A photography of the stones was

also taken and the shape of each stone images were approximate to an ellipse. Length and width of each stones were estimated using image processing and height were measured manually (Figure A3c). Both, stones and aluminium foil images, were binarized allowing to measure the number of black pixels of the black template to obtain a surface area per pixel conversion factor. The surface area of the aluminium foil (Figure A3d) were compute multiplying the number of pixels of the aluminium foil images by the conversion factor. The centroid of each stone were estimate using the *regionprops* function of MATLAB®. The major axis were found looking for the highest distance between to opposite points at the perimeter of each stone that connect a line passing through the centroid. The minor axis was defined as the perpendicular line to the mayor axis is passing through the centroid. The minor axis value was compute as the distance between the opposite points at the perimeter of each stone that belong to this line. The square root of the conversion factor was multiplied for each distance to convert pixels to cm units. An estimative of the surface area were obtained with each method: 603.19 cm^2 for the aluminium foil surface area, 640.80 cm^2 using Equation (A1) and 628.40 cm^2 with Equation (A2). When comparing the values obtaining with equations, these show percentage errors of 6.26% and 4.23%, respectively, in comparison with the aluminium foil surface area. Because Equation (A2) leads to smaller error it was used to compute the surface area of a large sample of 830 g of pumice stones oven dry of size 34.9–45.0 mm and 683.5 g of size 45.0–55.5 mm (Figure A3e,f), obtaining a surface area per mass unit of respectively. The specific surface area in m^{-1} units was compute multiplying the surface area per mass unit by the weight of the material used to fill the pad and divided by the volume of the pad. Table A2 summarized the data used to compute the specific surface area of pad built.

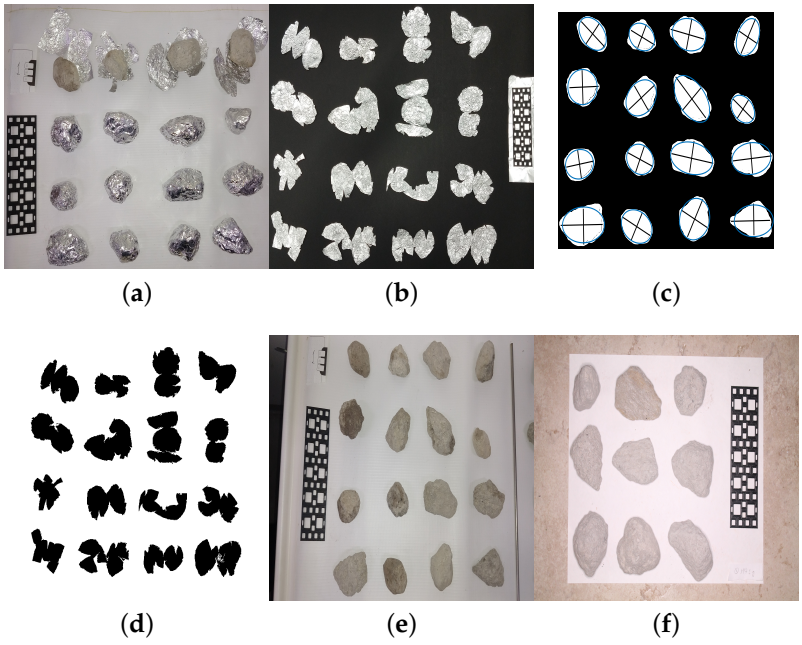

Figure A3. Sample of photographies and images used in the surface area compute process for the pumice stones. (**a**) Pumice stones of 3.5 to 4.5 mm cover with aluminium foil. (**b**) Photography of aluminium foil layers. (**c**) Ellipse approximation of each pumice stone for 34.9–45.0 mm size. (**d**) Binarized image of the aluminium foil layers. (**e**) Sample of photography for pumice stones of 34.9–45.0 mm size and template. (**f**) Sample of photography for pumice stones of 45.0–55.0 mm size and template.

Table A2. Summary of data used to compute the specific surface area of pads built with pumice stone material.

Particle size	34.9–45.0 mm	45.0–55.5 mm
Surface area per mass unit [m^2 kg^{-1}]	0.3329	0.2970
Weight of pad [kg]	10.428	10.310
Pad volume [m^3]	0.02718	0.02718
Specific surface area [m^{-1}]	127.72	112.65

Appendix B. Response Surface Plots

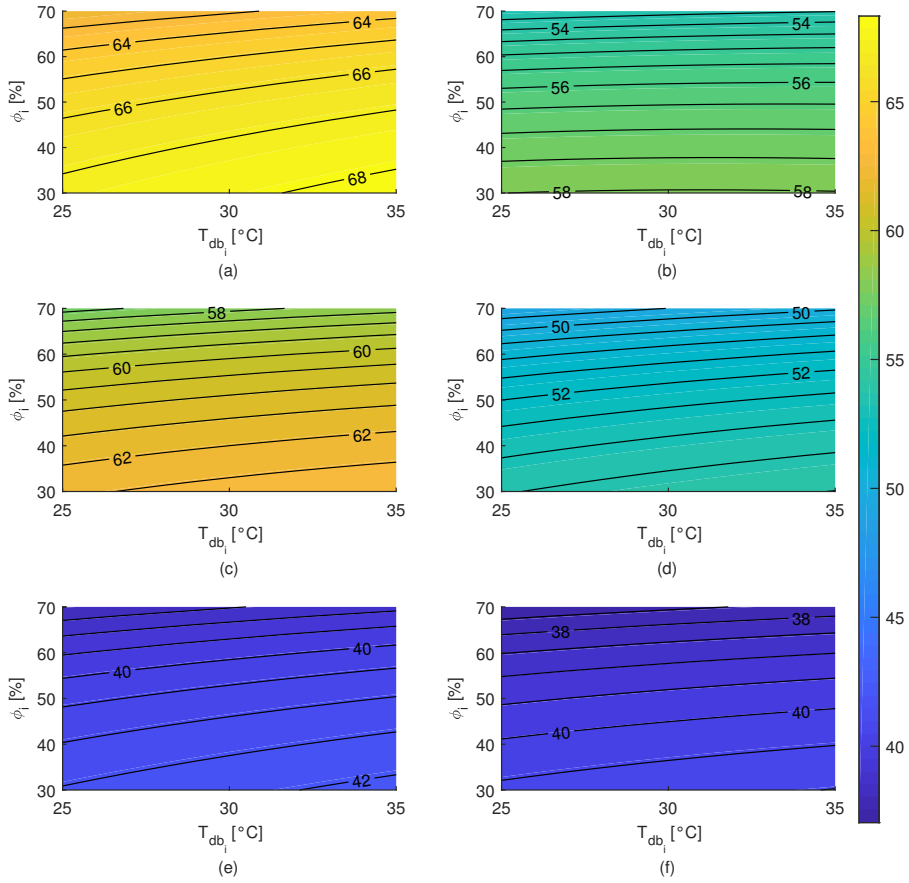

Figure A4. Pad cooling efficiency as a function of dry-bulb temperature of inlet air (T_{db_i}) and relative humidity (ϕ_i) for the pad materials studied. (**a**) Cellulose. (**b**) Small coconut shell (7.9–12.7 mm). (**c**) Big coconut shell (12.7–19.0 mm). (**d**) Burnt-clay bricks (12.7–19.0 mm). (**e**) Small pumice stones (34.9–45.0 mm). (**f**) Big pumice stones (45.0–55.5 mm).

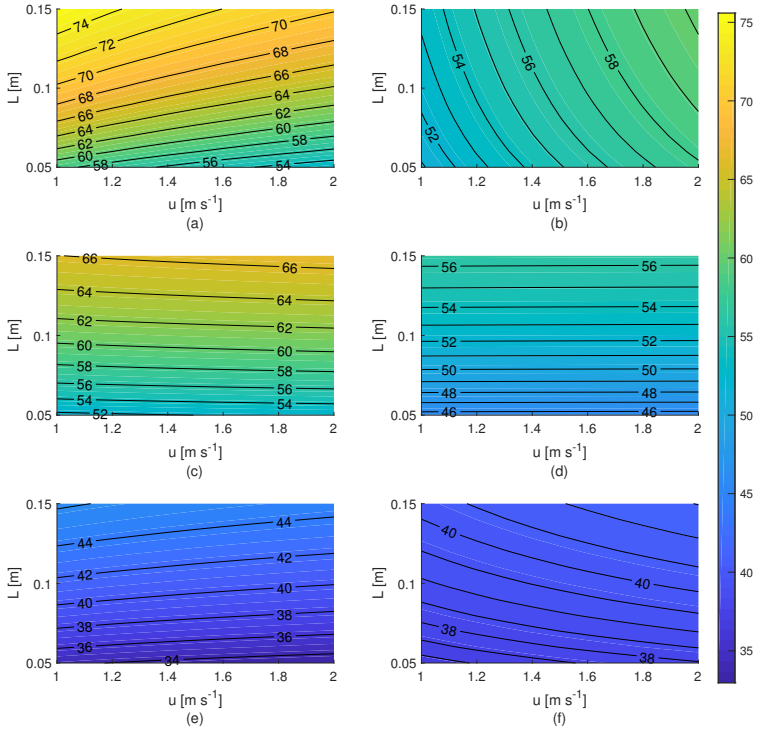

Figure A5. Pad cooling efficiency as a function of inlet air velocity (u) and pad thickness (L) for the pad materials studied. (**a**) Cellulose. (**b**) Small coconut shell (7.9–12.7 mm). (**c**) Big coconut shell (12.7–19.0 mm). (**d**) Burnt-clay bricks (12.7–19.0 mm). (**e**) Small pumice stones (34.9–45.0 mm). (**f**) Big pumice stones (45.0–55.5 mm).

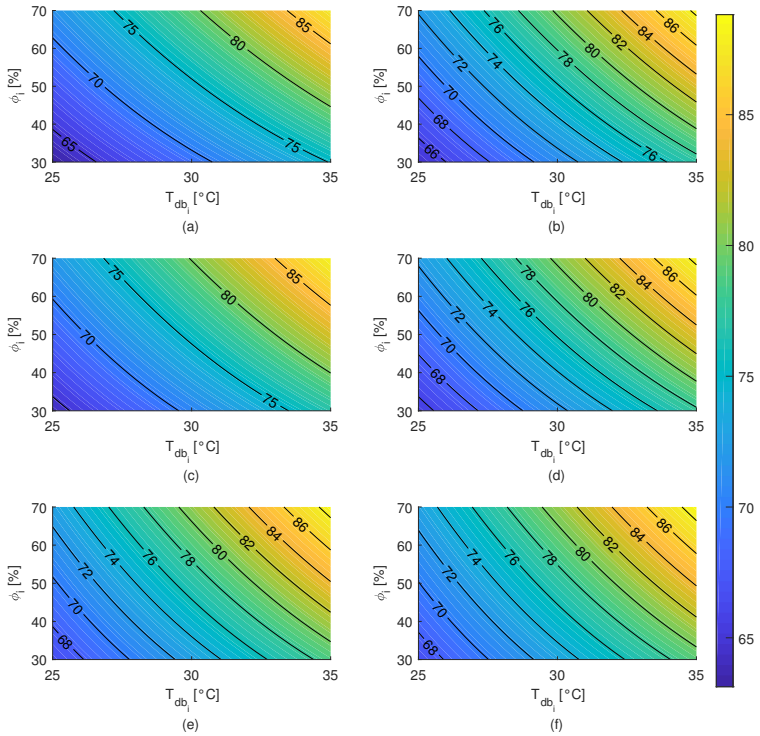

Figure A6. Temperature–Humidity Index at outlet par air conditions as a function of dry-bulb temperature of inlet air (T_{db_i}) and relative humidity (ϕ_i) for the pad studied. (**a**) Cellulose. (**b**) Small coconut shell (7.9–12.7 mm). (**c**) Big coconut shell (12.7–19.0 mm). (**d**) Burnt-clay bricks (12.7–19.0 mm). (**e**) Small pumice stones (34.9–45.0 mm). (**f**) Big pumice stones (45.0–55.5 mm).

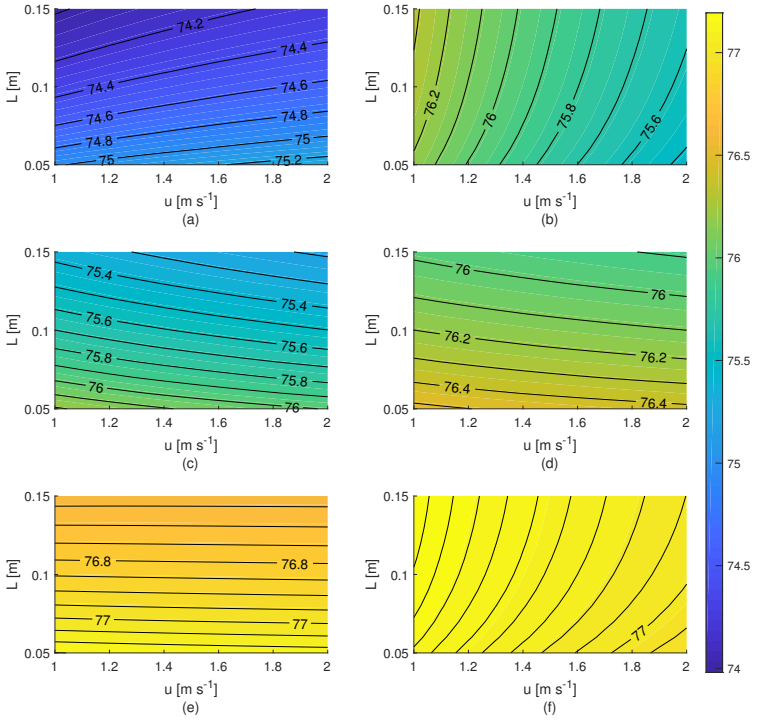

Figure A7. Temperature-Humidity Index (THI) at outlet pad air conditions as a function of inlet air velocity (u) and pad thickness (L) for the pad materials studied. (**a**) Cellulose. (**b**) Small coconut shell (7.9–12.7 mm). (**c**) Big coconut shell (12.7–19.0 mm). (**d**) Burnt-clay bricks (12.7–19.0 mm). (**e**) Small pumice stones (34.9–45.0 mm). (**f**) Big pumice stones (45.0–55.5 mm).

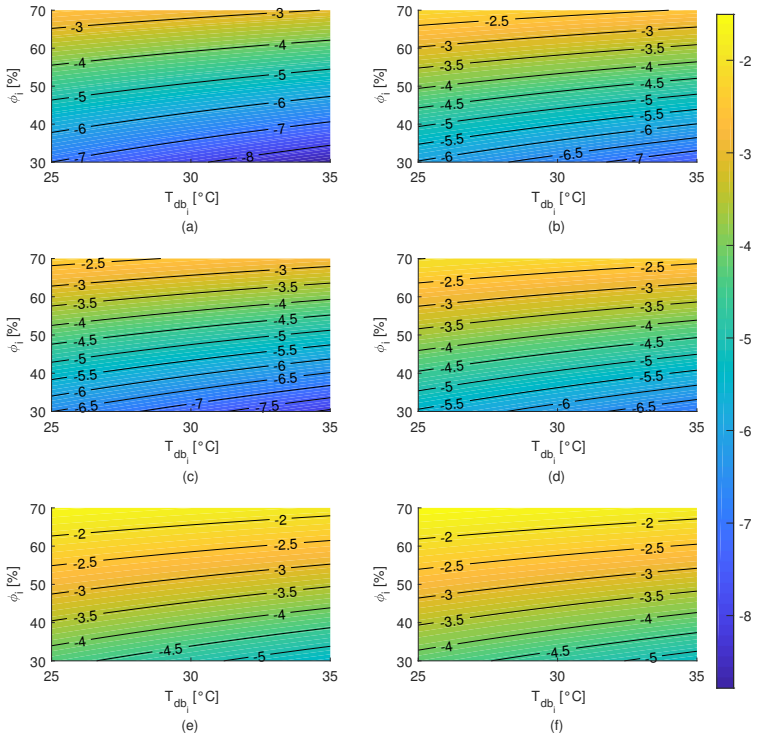

Figure A8. Difference between the outlet and inlet pad air dry-bulb temperature (ΔT) as a function of dry-bulb temperature of inlet air (T_{db_i}) and relative humidity (ϕ_i) for the pad materials studied. (**a**) Cellulose. (**b**) Small coconut shell (7.9–12.7 mm). (**c**) Big coconut shell (12.7–19.0 mm). (**d**) Burnt-clay bricks (12.7–19.0 mm). (**e**) Small pumice stones (34.9–45.0 mm). (**f**) Big pumice stones (45.0–55.5 mm).

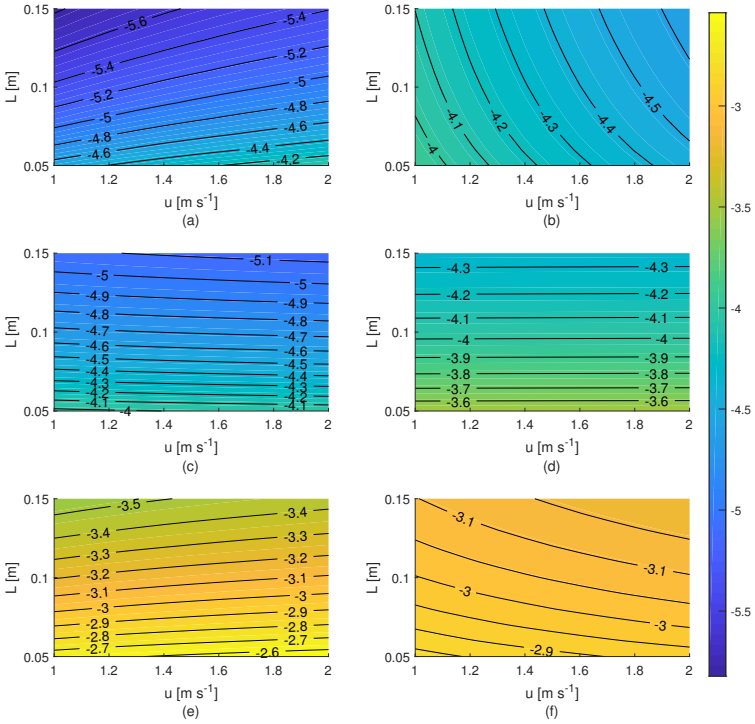

Figure A9. Difference between the outlet and inlet pad air dry-bulb temperature (ΔT) as a function of inlet air velocity (u) and pad thickness (L) for the pad materials studied. (**a**) Cellulose. (**b**) Small coconut shell (7.9–12.7 mm). (**c**) Big coconut shell (12.7–19.0 mm). (**d**) Burnt-clay bricks (12.7–19.0 mm). (**e**) Small pumice stones (34.9–45.0 mm). (**f**) Big pumice stones (45.0–55.5 mm).

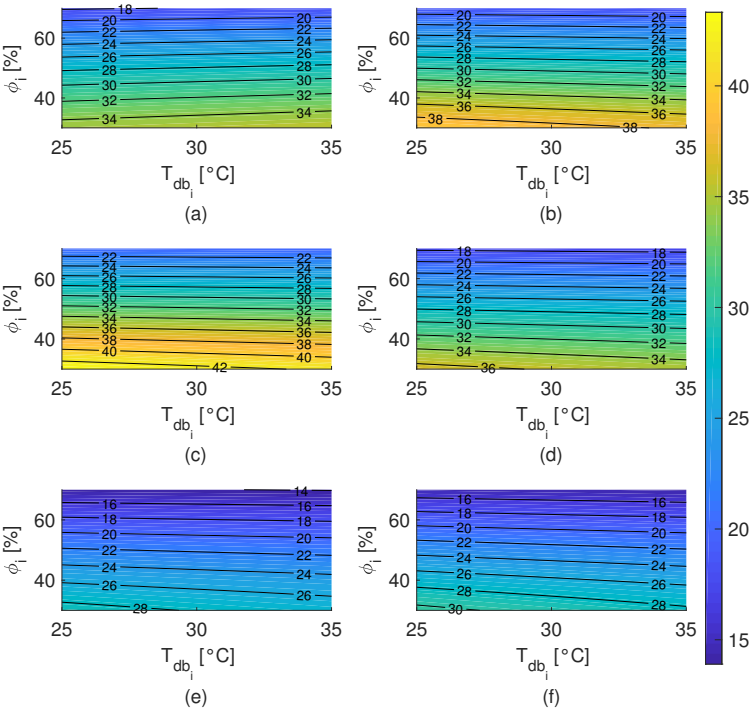

Figure A10. Difference between the outlet and inlet pad air relative humidity ($\Delta\phi$) as a function of dry-bulb temperature of inlet air (T_{db_i}) and relative humidity (ϕ_i) for the pad materials studied. (**a**) Cellulose. (**b**) Small coconut shell (7.9–12.7 mm). (**c**) Big coconut shell (12.7–19.0 mm). (**d**) Burnt-clay bricks (12.7–19.0 mm). (**e**) Small pumice stones (34.9–45.0 mm). (**f**) Big pumice stones (45.0–55.5 mm).

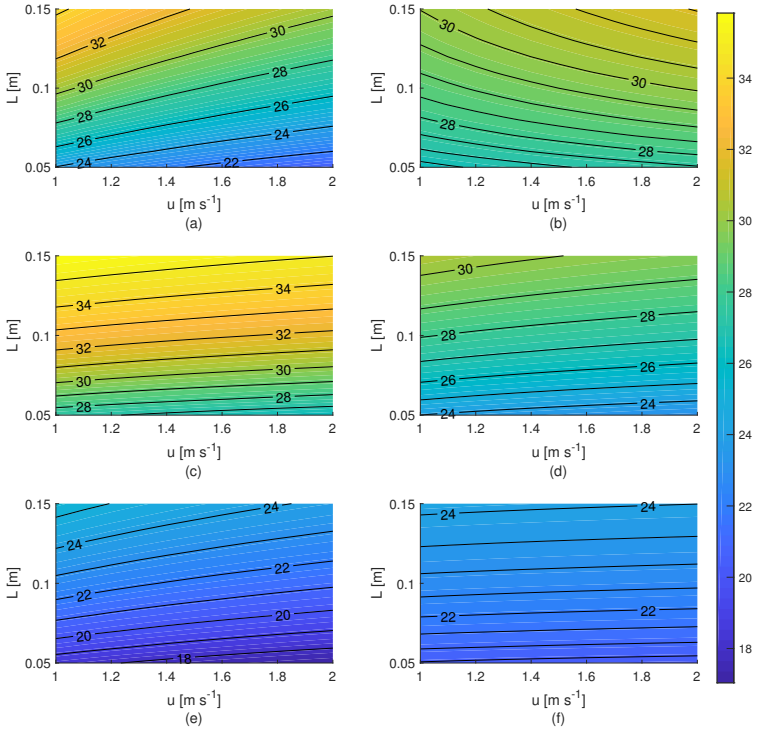

Figure A11. Difference between the outlet and inlet pad air relative humidity ($\Delta\phi$) as a function of inlet air velocity (u) and pad thickness (L) for the pad materials studied. (**a**) Cellulose. (**b**) Small coconut shell (7.9–12.7 mm). (**c**) Big coconut shell (12.7–19.0 mm). (**d**) Burnt-clay bricks (12.7–19.0 mm). (**e**) Small pumice stones (34.9–45.0 mm). (**f**) Big pumice stones (45.0–55.5 mm).

References

1. Malli, A.; Seyf, H.R.; Sharifian, S.; Layeghi, M.; Behravesh, H. Investigating the performance of cellulosic evaporative cooling pads. *Energy Convers. Manag.* **2011**, *52*, 2598–2603. [CrossRef]
2. López, A.; Valera, D.L.; Molina-Aiz, F.D.; Peña, A. Sonic anemometry to evaluate airflow characteristics and temperature distribution in empty Mediterranean greenhouses equipped with pad-fan and fog systems. *Biosyst. Eng.* **2012**, *113*, 334–350. [CrossRef]
3. Laknizi, A.; Mahdaoui, M.; Ben Abdellah, A.; Anoune, K.; Bakhouya, M.; Ezbakhe, H. Performance analysis and optimal parameters of a direct evaporative pad cooling system under the climate conditions of Morocco. *Case Stud. Therm. Eng.* **2019**, *13*, 100362. [CrossRef]
4. Chinenye, N.M.; Manuwa, S.I. Review of research and application of evaporative cooling in preservation of fresh agricultural produce. *Int. J. Agric. Biol.* **2014**, *7*, 85–102. [CrossRef]
5. Dhamneya, A.K.; Rajput, S.P.; Singh, A. Thermodynamic performance analysis of direct evaporative cooling system for increased heat and mass transfer area. *Ain Shams Eng. J.* **2018**, *9*, 2951–2960. [CrossRef]
6. Maurya, R.; Shrivastava, N.; Shrivastava, V. Performance evaluation of alternative evaporative cooling media. *Int. J. Sci. Eng. Res.* **2014**, *5*, 676–684.
7. Jain, J.K.; Hindoliya, D.A. Experimental performance of new evaporative cooling pad materials. *Sustain. Cities Soc.* **2011**, *1*, 252–256. [CrossRef]
8. Kulkarni, R.K.; Rajput, S.P.S. Comparative performance analysis of evaporative cooling pads of alternative configurations and materials. *Int. J. Adv. Eng. Technol.* **2013**, *6*, 1524–1534.
9. Vala, K.; Kumpavat, M.; Nema, A. Comparative Performance Evaluation of Evaporative Cooling Local Pad materials with Commercial Pads. *Int. J. Eng. Trends Technol.* **2016**, *39*, 198–203. [CrossRef]
10. Akintunji, L.L.; Haruna, I.U.; Momoh, B.S. Theoretical performance analysis of coconut coir as media in evaporative coolers. *Int. J. Sci. Technol. Res.* **2014**, *3*, 310–315.
11. Khond, V. Experimental investigation of desert cooler performance using four different cooling pad materials. *Am. J. Sci. Ind. Res.* **2011**, *2*, 418–421. [CrossRef]
12. Shekhar, S.; Suman, S.; Moharana, H.S.; Sethy, D. Performance of Different Pad Materials in Advanced Desert Coolers—A Comparative Study. *Int. J. Eng. Sci.* **2016**, *4368*, 250–254.
13. Liao, C.M.; Singh, S.; Wang, T.S. Characterizing the performance of alternative evaporative cooling pad media in thermal environmental control applications. *J. Environ. Sci. Health Part A* **1998**, *33*, 1391–1417. [CrossRef]

14. Vijaykumar, K.N.; Kulkarni, M.M.; Jadhav, N.A.; Bhor, M.J.; Shinde, S.S. Experimental performance evaluation of new cooling pad material for direct evaporating cooling for pune summer conditions. *Int. J. Eng. Trends Technol. (IJETT)* **2015**, *22*, 281–287.
15. Vigoderis, R.B.; Ferreira Tinoco, I.D.F.; de Lacerda Filho, A.F.; Nogueira da Silva, J.; Gates, R.S.; de Pauli, D.G.; da Silva, C.E.; de Carvalho, M.C. Construção de túnel de vento reduzido, visando a avaliação de argila expandida em sistemas de resfriamento adiabático evaporativo para arrefecimento térmico em galpões de produção animal. *Eng. Agric.* **2007**, *15*, 191–199.
16. Osorio, J.A.; Ferreira, I.D.F.; Oliveira, K.S.; Martins, M.A.; Damasceno, F.A. Validation of a CFD model for prediction of the efficiency of evaporative cooling in porous panel. *Rev. UDCA Actual. Divulg. Cient.* **2012**, *15*, 209–217. [CrossRef]
17. Al-Sulaiman, F. Evaluation of the performance of local fibers in evaporative cooling. *Energy Convers. Manag.* **2002**, *43*, 2267–2273. [CrossRef]
18. Abohorlu Doğramacı, P.; Riffat, S.; Gan, G.; Aydın, D. Experimental study of the potential of eucalyptus fibres for evaporative cooling. *Renew. Energy* **2019**, *131*, 250–260. [CrossRef]
19. Doğramacı, P.A.; Aydın, D. Comparative experimental investigation of novel organic materials for direct evaporative cooling applications in hot-dry climate. *J. Build. Eng.* **2020**, *30*, 101240. [CrossRef]
20. Wijaksana, H.; Winaya, I.N.S.; Sucipta, M.; Ghurri, A.; Suarnadwipa, N. The investigation on cooling capacity and CELdek material pad classification of evaporative cooling pad system using different pad material with water temperature and water discharge variations. *AIP Conf. Proc.* **2018**, *1983*, 1–7. [CrossRef]
21. Kulkarni, R.K.; Rajput, S.P.S. Theoretical performance analysis of jute fiber rope bank as media in evaporative coolers. *Indian J. Sci. Technol.* **2010**, *3*, 1075–1080. [CrossRef]
22. Olukunle, J.; Ndukwu, M.C.; Manuwa, S.I.; Oluwalana, I.B. Analyses of Some Local Material as a possible cooling pad in Active Evaporative Cooling System. *Balk. Agric. Eng. Rev.* **2013**, *18*, 11–19.
23. Basiouny, M.A.; Abdallah, S.E. Influence of pad configuration on evaporative cooling system effectiveness inside a wind tunnel. *AMA Agric. Mech. Asia Afr. Lat. Am.* **2013**, *44*, 70–81.
24. Elmsaad, E.; Omran, A. Evaluating the effect of new Local materials of evaporative cooling pads. *Am.-Eurasian J. Agric. Environ.* **2015**, *15*, 78–84. [CrossRef]
25. Ahmed, E.M.; Abaas, O.; Ahmed, M.; Ismail, M.R. Performance evaluation of three different types of local evaporative cooling pads in greenhouses in Sudan. *Saudi J. Biol. Sci.* **2011**, *18*, 45–51. [CrossRef] [PubMed]
26. Liao, C.M.; Chiu, K.H. Wind tunnel modeling the system performance of alternative evaporative cooling pads in Taiwan region. *Build. Environ.* **2002**, *37*, 177–187. [CrossRef]
27. Gunhan, T.; Demir, V.; Yagcioglu, A.K. Evaluation of the suitability of some local materials as cooling pads. *Biosyst. Eng.* **2007**, *3*, 369–377. [CrossRef]
28. Martínez, P.; Ruiz, J.; Martínez, P.J.; Kaiser, A.S.; Lucas, M. Experimental study of the energy and exergy performance of a plastic mesh evaporative pad used in air conditioning applications. *Appl. Therm. Eng.* **2018**, *138*, 675–685. [CrossRef]
29. Cui, X.; Yan, W.; Liu, Y.; Zhao, M.; Jin, L. Performance analysis of a hollow fiber membrane-based heat and mass exchanger for evaporative cooling. *Appl. Energy* **2020**, *271*, 115238. [CrossRef]
30. Laknizi, A.; Ben Abdellah, A.; Faqir, M.; Essadiqi, E.; Dhimdi, S. Performance characterization of a direct evaporative cooling pad based on pottery material. *Int. J. Sustain. Eng.* **2021**, *14*, 46–56. [CrossRef]
31. Franco, A.; Valera, D.L.; Peña, A. Energy efficiency in greenhouse evaporative cooling techniques: Cooling boxes versus cellulose pads. *Energies* **2014**, *7*, 1427–1447. [CrossRef]
32. Obando, F.A.; Montoya, A.P.; Osorio, J.A.; Damasceno, F.A.; Norton, T. Evaporative pad cooling model validation in a closed dairy cattle building. *Biosyst. Eng.* **2020**, *198*, 147–162. [CrossRef]
33. Kovacevic, I.; Sourbron, M. The numerical model for direct evaporative cooler. *Appl. Therm. Eng.* **2017**, *113*, 8–19. [CrossRef]
34. Incropera, F.P.; Dewitt, D.P.; Lavine, A.S.; Bergman, T.L. *Fundamentals of Heat and Mass Transfer*, 7th ed.; John Wiley & Sons, Ltd.: Hoboken, NJ, USA, 2011; p. 1076.
35. Dowdy, J.A.; Karabash, N.S. Experimental Determination of Heat and Mass Transfer Coefficients in rigid Impregnated Cellulose Evaporative Media. *ASHRAE Trans.* **1987**, *93*, 382–395.
36. Franco, A.; Valera, D.L.; Madueño, A.; Peña, A. Influence of water and air flow on the performance of cellulose evaporative cooling pads used in mediterranean greenhouses. *Trans. ASABE* **2010**, *53*, 565–576. [CrossRef]
37. Camargo, J.R.; Ebinuma, C.D.; Silveira, J.L. Experimental performance of a direct evaporative cooler operating during summer in a Brazilian city. *Int. J. Refrig.* **2005**, *28*, 1124–1132. [CrossRef]
38. Sachdeva, A.; Rajput, S.P.S.; Kothari, A. Performance Analysis of Direct Evaporative Cooling in Indian summer. *Int. J. Res. Aeronaut. Mech.* **2015**, *3*, 132.
39. Sayed, E.; Khater, G. Performance of Direct Evaporative Cooling System under Egyptian Conditions. *Climatol. Weather. Forecast.* **2014**, *31*, 1595–1620. [CrossRef]
40. Wang, C.; Cao, W.; Li, B.; Shi, Z.; Geng, A. A fuzzy mathematical method to evaluate the suitability of an evaporative pad cooling system for poultry houses in China. *Biosyst. Eng.* **2008**, *101*, 370–375. [CrossRef]
41. Xu, J.; Li, Y.; Wang, R.Z.; Liu, W.; Zhou, P. Experimental performance of evaporative cooling pad systems in greenhouses in humid subtropical climates. *Appl. Energy* **2015**, *138*, 291–301. [CrossRef]
42. Elmetenani, S.; Yousfi, M.; Merabeti, L.; Belgroun, Z.; Chikouche, A. Investigation of an evaporative air cooler using solar energy under Algerian climate. *Energy Procedia* **2011**, *6*, 573–582. [CrossRef]

43. Chinenye, N.M.; Manuwa, S.I.; Olukunle, O.J.; Oluwalana, I.B. Development of an active evaporative cooling system for short-term storage of fruits and vegetable in a tropical climate. *Agric. Eng. Int. CIGR J.* **2013**, *15*, 307–313.
44. He, S.; Guan, Z.; Gurgenci, H.; Hooman, K.; Lu, Y.; Alkhedhair, A.M. Experimental study of film media used for evaporative pre-cooling of air. *Energy Convers. Manag.* **2014**, *87*, 874–884. [CrossRef]
45. NOOA. *Livestock Hot Weather Stress. Operations Manual Letter C-31-76*; Technical Report; National Oceanic and Atmospheric Administration: Kansas City, MO, USA, 1976.
46. ASHRAE. *ASHRAE Handbook HVAC Systems and Equipment*; Ashrae, American Society of Heating, Refrigeration and Air-Conditioning Engineers, Inc.: Atlanta, GA, USA, 2008.
47. Thom, E.C. The Discomfort Index. *Weatherwise* **1959**, *12*, 57–61. [CrossRef]
48. Bergey, E.A.; Getty, G.M. A review of methods for measuring the surface area of stream substrates. *Hydrobiologia* **2006**, *556*, 7–16. [CrossRef]
49. Wilcoxon, F. Individual Comparisons by Ranking Methods. *Biom. Bull.* **1945**, *1*, 80–83. [CrossRef]
50. Paulson, D.S. Nonparametric Statistical Methods. In *Biostatistics and Microbiology: A Survival Manual*; Paulson, D.S., Ed.; Springer: New York, NY, USA, 2009; Chapter 7, pp. 121–162. [CrossRef]
51. The MathWorks, Inc. *Statistics and Machine Learning Toolbox User's Guide*; The MathWorks, Inc.: Natick, MA, USA, 2020.
52. Sheng, C.; Agwu Nnanna, A.G. Empirical correlation of cooling efficiency and transport phenomena of direct evaporative cooler. *Appl. Therm. Eng.* **2012**, *40*, 48–55. [CrossRef]
53. Kundu, P.; Kumar, V.; Mishra, I.M. Experimental and numerical investigation of fluid flow hydrodynamics in porous media: Characterization of pre-Darcy, Darcy and non-Darcy flow regimes. *Powder Technol.* **2016**, *303*, 278–291. [CrossRef]
54. The MathWorks, Inc. *Curve Fitting Toolbox: For Use with MATLAB®: User Guide*; The MathWorks, Inc.: Natick, MA, USA, 2001.
55. Laberge, B.; Rousseau, A.N. Rethinking environment control strategy of confined animal housing systems through precision livestock farming. *Biosyst. Eng.* **2017**, *155*, 96–123. [CrossRef]
56. Franco, A.; Valera, D.L.; Peña, A.; Pérez, A.M. Aerodynamic analysis and CFD simulation of several cellulose evaporative cooling pads used in Mediterranean greenhouses. *Comput. Electron. Agric.* **2011**, *76*, 218–230. [CrossRef]
57. Chen, X.; Su, Y.; Aydin, D.; Ding, Y.; Zhang, S.; Reay, D.; Riffat, S. A novel evaporative cooling system with a polymer hollow fibre spindle. *Appl. Therm. Eng.* **2018**, *132*, 665–675. [CrossRef]
58. Darwesh, M.; Abouzaher, S.; Fouda, T.; Helmy, M. Effect of using pad manufactured from agricultural residues on the performance of evaporative cooling system. *Jordan J. Agric. Sci.* **2007**, *24*, 1023–1043.
59. Kovács, L.; Kézér, F.L.; Póti, P.; Boros, N.; Nagy, K. Short communication: Upper critical temperature-humidity index for dairy calves based on physiological stress variables. *J. Dairy Sci.* **2020**, *103*, 2707–2710. [CrossRef] [PubMed]
60. The MathWorks, Inc. *Image Processing Toolbox User's Guide*; The MathWorks, Inc.: Natick, MA, USA, 2020.